Univerzita Karlova v Praze
Matematicko-fyzikální fakulta

BAKALÁŘSKÁ PRÁCE

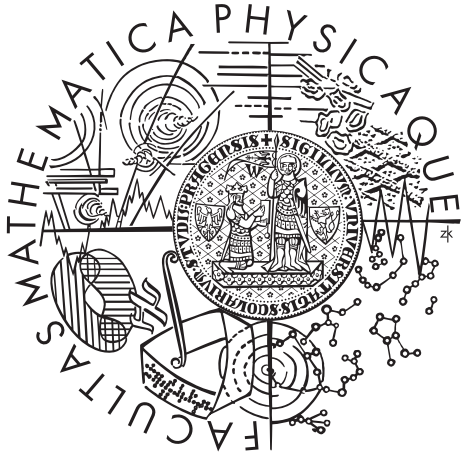

Marek Kozoň

Termální vývoj Saturnova měsíce Enceladu

Katedra geofyziky

Vedoucí bakalářské práce: Doc. RNDr. Ondřej Čadek, CSc.

Studijní program: Fyzika

Studijní obor: Obecná fyzika

Praha 2015

Charles University in Prague
Faculty of Mathematics and Physics

BACHELOR THESIS

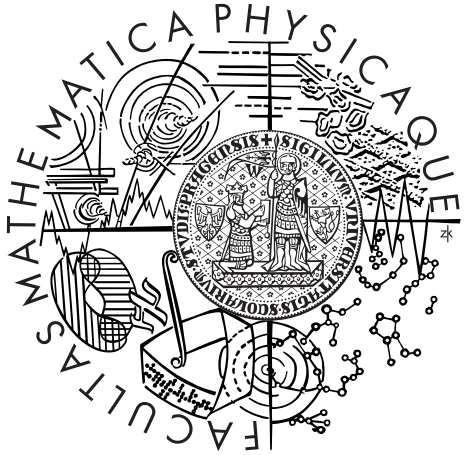

Marek Kozoň

Thermal Evolution of Saturn's Moon Enceladus

Department of Geophysics

Supervisor of the bachelor thesis: Doc. RNDr. Ondřej Čadek, CSc.

Study programme: Physics

Specialization: General Physics

Prague 2015

I declare that I carried out this bachelor thesis independently, and only with the cited sources, literature and other professional sources.

I understand that my work relates to the rights and obligations under the Act No. 121/2000 Coll., the Copyright Act, as amended, in particular the fact that the Charles University in Prague has the right to conclude a license agreement on the use of this work as a school work pursuant to Section 60 paragraph 1 of the Copyright Act.

In ..... date ..... signature of the author

I would like to thank my supervisor, Doc. RNDr. Ondřej Čadek, for his guidance, great patience, support and inspiration while introducing me in the world of science. I am also very thankful to all the lecturers and fellow students for creating such a pleasant and helpful atmosphere during my study. Last, but definitely not least, I thank my parents and grandparents for their enormous support through all my life.

Název práce: Termální vývoj Saturnova měsíce Enceladu

Autor: Marek Kozoň

Katedra: Katedra geofyziky

Vedoucí bakalářské práce: Doc. RNDr. Ondřej Čadek, CSc., Katedra geofyziky

Abstrakt: Študujeme termálny vývoj Enceladu na veľmi dlhých časových škálach. Na to využívame nami vytvorený program vo Fortrane, ktorý modeluje slapovú deformáciu a ňou spôsobenú tepelnú disipáciu ako aj transport tepla v telese za pomoci kondukcie. Započítaný je tiež efekt rozpadu dlho-žijúcich rádioaktívnych izotopov v jadre na tepelnú produkciu. V práci predstavujeme závislosť charakteru tepelného vývoja na minimálnej viskozite a rozdielnych hodnotách konštantnej excentiricity, pričom vybrané prípady sú skúmané detailnejšie. Poukazujeme, ďalej, na skutočnosť, že pri zahrnutí vývoja orbitálnej excentricity nemá jej počiatočná hodnota zásadný vplyv na výsledok termálneho vývoja a mesiac vždy rýchlo zamrzne. Nakoniec skúmame závislosť tepelného vývoja na veľkosti pridaného hydrotermálneho zdroja v jadre a ukazujeme, že je možné nájsť hodnotu jeho výkonu, pri ktorej satelit nezamrzne a ani sa neprehreje po dobu aspoň 4 miliárd rokov, čo je nutnou podmienkou pre zachovanie termálnej aktivity Enceladu od jeho vzniku až po súčasnosť.

Klíčová slova: Enceladus, slapy, excentricita, vývoj

Title: Thermal evolution of Saturn's moon Enceladus

Author: Marek Kozoň

Department: Department of Geophysics

Supervisor: Doc. RNDr. Ondřej Čadek, CSc., Department of Geophysics

Abstract: We study thermal evolution of Enceladus on very long time scales. In order to do so, we created a Fortran program modeling tidal deformation and thus induced heat dissipation as well as conductive transport of the heat in the body of the moon. Effect of long-lived radioactive isotopes decay in the core on the heat generation is included. We show the dependence of a thermal scenario character on different minimal viscosity and constant eccentricity values and study chosen cases in detail. We further demonstrate that, if orbital eccentricity evolution is incorporated, its initial value has no essential effect on the thermal evolution result, with the body always freezing quickly. Lastly, we examine the dependence of a thermal scenario on added values of hydrothermal heating power from the core and present that a power magnitude can be found, with which the satellite does not freeze, nor overheats in the first 4 billions of years what is necessary for maintaining a thermal activity on Enceladus since its formation to the present time.

Keywords: Enceladus, tides, eccentricity, evolution

Contents

Introduction

Planet Saturn has been known to mankind already since the ancient times. It was, however, first with the invention of telescope, in the 17th century, that its magnificent rings were observed for the first time and the first of its moons discovered. Since then, the exploration has continued with gradually more and more precise observations from Earth, as well as with the help of robotic spacecrafts *Pioneer 11* and *Voyager 1* and *2*, later on. In the last decade, the investigation of Saturn and its moons has experienced a great boost thanks to the *Cassini* spacecraft which has arrived to the planet, along with the robotic lander *Huygens*, in 2004 and provides us with a massive amount of data since then.

One of the most spectacular achievements of the spacecraft was the observation of plume of gas and ice particles erupting from the south pole of Enceladus, a small but very bright icy moon of Saturn. Furthermore, it was discovered that the south pole is much warmer than had been expected. The discovery of active cryovolcanism has suddenly put tiny Enceladus into the spotlight of research and brought up many thought-provoking questions: How does the mechanism of the geysers work? How is the energy generated and transported? Is there a subsurface liquid water reservoir? Could there possibly thrive a microbial life?

It is now widely assumed that the energy is generated on Enceladus via tidal deformation of its icy mantle generated by changing intensity of gravitation from Saturn as the moon travels along its eccentric orbit, enhanced by a subsurface ocean of some kind [1] and perhaps some hydrothermal processes in the core [2]. Albeit, there still exist only indirect proofs of the water reservoir and it is, therefore, extremely important to learn more about the thermal mechanisms as well as about the structure and history of the moon. One way to do so is examination of the data obtained by *Cassini* during its numerous flybys of the moon, although, there is also an another, very powerful tool: computer modeling.

In order to contribute to the knowledge of icy moons, we created a computer program in Fortran calculating viscoelastic tidal deformation in the mantle of Enceladus and power dissipated that way. Heat transport by conduction is taken into account in order to evaluate temperature distribution in the body of the moon. Long-lived radioactive isotopes decay as a heat source in the core was included. In later phase, we incorporated orbital eccentricity evolution as well as another constant homogeneous heat source, representing hydrothermal processes, in the core. Our goal was to examine thermal evolution of Enceladus on very long time scales and its dependence on various parameters, with a prospect of discovering a long-term stable scenario of sufficiently large thermal activity.

The thesis has the following structure: In the first chapter, a general overview of our current knowledge of Enceladus is provided. The second one explains the mathematical model used, from equations of viscoelasticity through dissipation and eccentricity change computation to heat conduction equation and radioactive power sources. The third one is concerned with its numerical implementation, including a description of validation tests. In the fourth chapter, the results of the simulations for constant and time-variable eccentricity are presented, followed by a discussion. We also provide a brief appendix summarizing some of the more advanced mathematics and mathematical identities we used.

1. Enceladus

Enceladus (figure 1.1), only 504 km in diameter, is one of six mid-sized moons orbiting Saturn. It was discovered by William Herschel in 1789 and its name stems from one of the Giants of the ancient Greek mythology, who was, according to the myth, crushed by the goddess Athene and buried under the island of Sicily [3]. Despite its size, the tiny moon belongs to the most interesting objects in the Solar System, both from the planetological and the astrobiological view. It has been thoroughly studied by the *Cassini* probe for the last decade, what led to numerous impressive discoveries. In this chapter, we provide a brief description of Enceladus and its most important characteristics. The source of information for this chapter is, except when cited otherwise, [1].

Enceladus orbits Saturn in the distance of about 238 000 km [4]. Due to tidal lock to the planet, it exhibits synchronous rotation, always facing Saturn the same side. Furthermore, it is in 2:1 eccentricity type orbital resonance with another moon, Dione.

The density measurements suggest about 60:40 rock:ice mixture by mass for Enceladus. It is widely believed that its body is differentiated, with icy mantle and metal-silicate core, however, the final proof is still missing for this. Geologically, the surface of Enceladus is remarkably symmetrical about both the rotational axis and the direction to Saturn. One of its remarkable features is the highest albedo in the Solar System reflecting about 80 % of the intercepted sunlight. It also hosts a wide variety of terrain types, while, generally, the surface is relatively young. The oldest regions form a band from the Saturn-facing side, over the north pole to the anti-Saturn side and are highly cratered, albeit the craters have been modified by tectonic fractures, viscous relaxation and burial since their formation. Regions around the centers of the leading and trailing hemispheres incorporate ridges and grooves, which often run parallel to each other. The cratered and ridged terrain types transition into each other very quickly, forming exotic landscapes (figure 1.2). All of the mentioned above suggests some geological activity in the recent past.

The South Polar Terrain is a region of southern latitudes greater than 50°, bounded by arcs of scarps and ridges. The lack of craters suggests this area is not older than a few million years. It is right at the center of it, where the most prominent structures of Enceladus, the tiger stripes, occur. These are a set of four parallel fractures about 130 km long and spaced 35 km apart, each fenced by ridges at both sides. The tiger stripes are the source of plume jets (figure 1.3) and thermal emission (figure 1.4) as observed by *Cassini*.

There are two types of jets erupting from the tiger stripes. The gas jets consist mostly of water but there is also some CO_2, CH_4, NH_3, heavier hydrocarbons and organic molecules. On the other hand, the particle geysers are mostly composed of water ice with about 1 % of salt. The both jets combine into a merged plume in high altitude. It is assumed that most of the gas and about 10 % of the particles reach the escape velocity and leave Enceladus. The escaped particles are believed to feed the E ring of Saturn (figure 1.5) and there are speculations that the water vapor from Enceladus could be a major source of oxygen in the atmospheres of Titan and Saturn. The rest of the grains falls back on the surface of the moon,

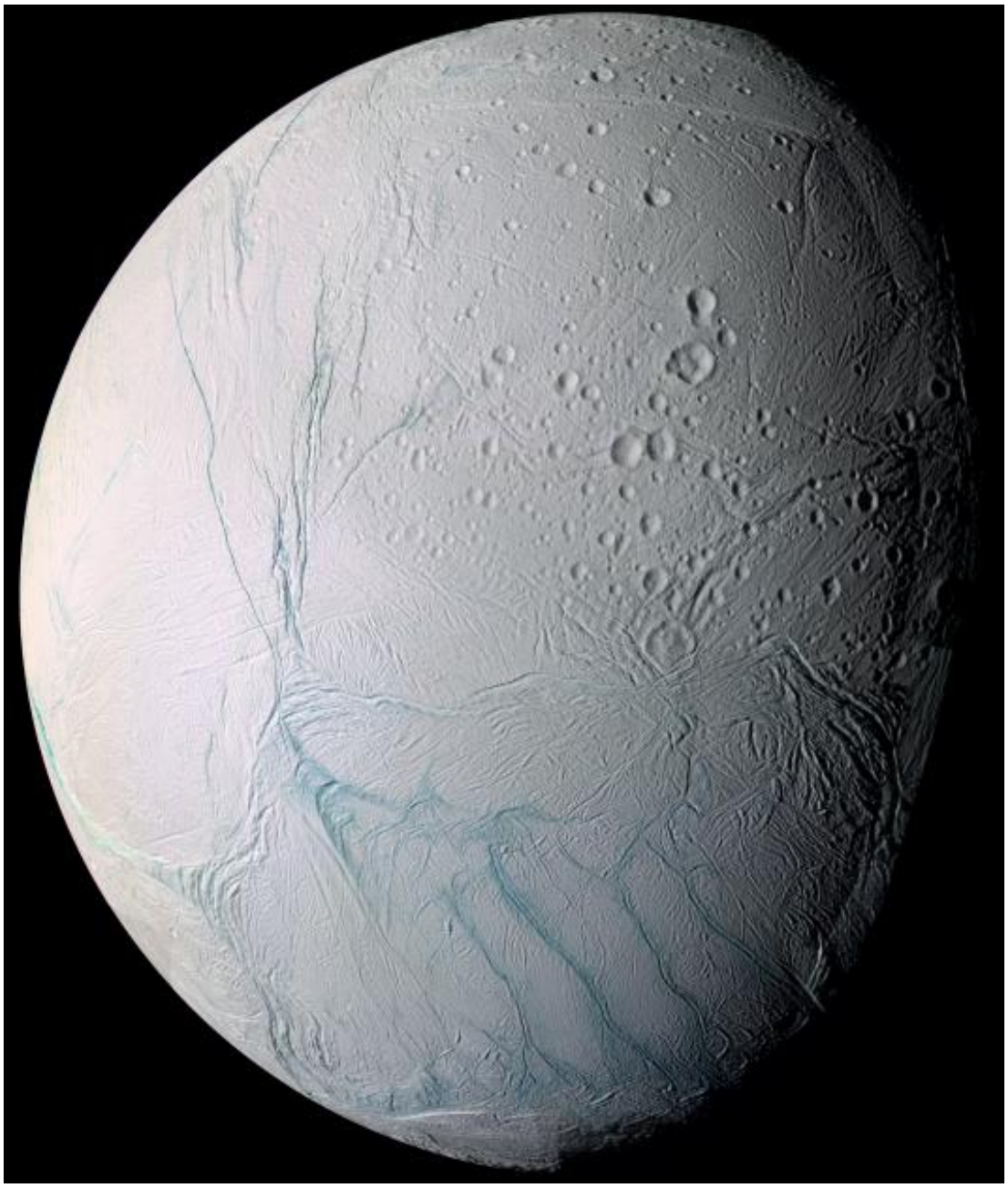

Figure 1.1: Enceladus. The composite, false-color image including various wavelengths, from ultraviolet to infrared, provides a view of the anti-Saturn hemisphere of Enceladus. Old, cratered terrain can be seen in the upper right, transitioning into younger area rich in fractures and ridges on the left. The four tiger stripes of the south pole dominate the lower part of the image. *The source of all the figures in this chapter and their descriptions is [5].*

Figure 1.2: Transition. The image, taken in visible light, shows a transition between older, cratered and younger, fractured terrain in detail. The prominent fracture in the center is probably one the youngest features in this view.

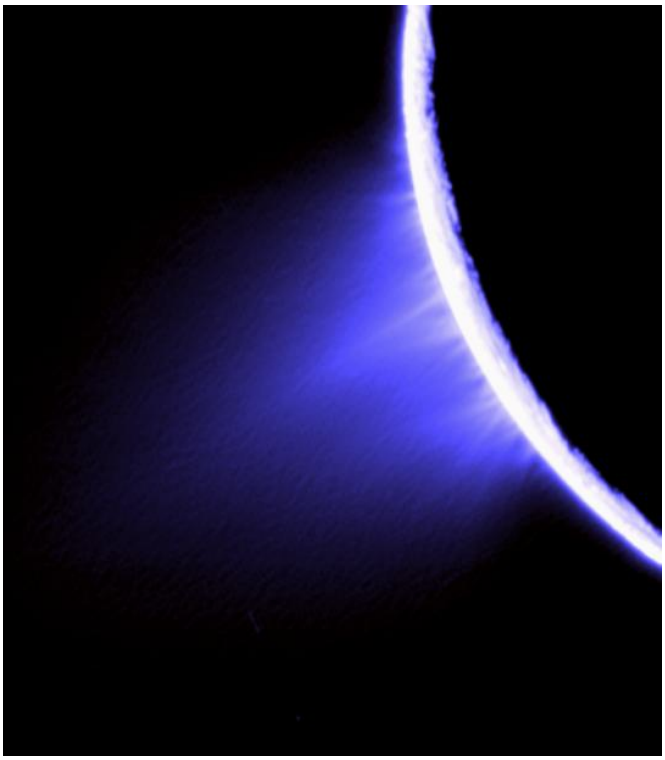

Figure 1.3: Plume. This is a false-color image of the plume of gas and ice particles over the Enceladus' south pole. Visibility of individual erupting jets is enhanced.

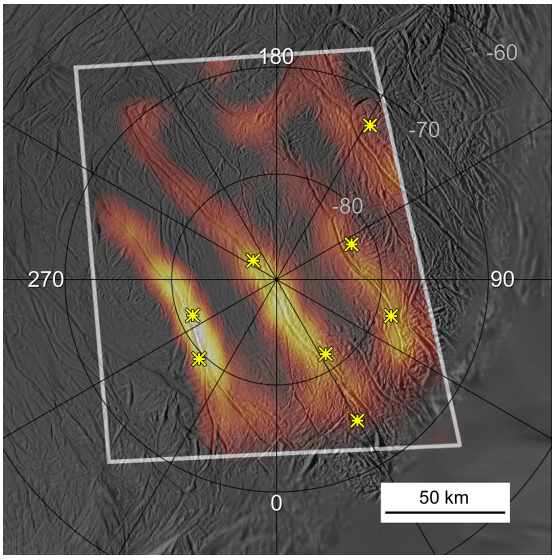

Figure 1.4: Hot tiger stripes. The image consists of an infrared scan of the south polar area superimposed on a grayscale mosaic of the region. Latitude and longitude are indicated by the numbers. The stars annotate the locations of the plume jets and it is clearly visible that these are the places where the most heat is radiated. The hottest registered temperature by the scan was at least 180 K. Apart from the four dominant tiger stripes, there are additional warm spots seen in the upper right.

causing the already mentioned high albedo and crater burial.

The *Cassini* thermal emission measurements show that the temperatures within the troughs are at least 180 K and they radiate the total power of about 16 GW, however, the latter value incorporates a rather large uncertainty. It is generally believed that, for Enceladus, the main mechanism of power generation is tidal heating. Albeit, the details of the heat production and transportation within the body of the moon still remain unclear. Tidal heating in the silicate core is almost certainly negligible, due to the high silicate rigidity and viscosity, however, some power is produced here via radioactive decay. It also seems that such great dissipated power as mentioned above is not achievable with the deformation limited by the ice shell coupled directly to the core, therefore, it is assumed that the existence of at least a regional subsurface water ocean at the core-mantle boundary (CMB) is necessary. Although, this raises another question of how such a sea could sustain over geological ages. Even with high concentration of ammonia, which has been detected in the plumes and could serve as an antifreeze substance, this seems to be very difficult for a global ocean. On the other hand, a regional body of water restrained to the area under the south polar region looks more plausible and would also be consistent with the slight depression of the southern polar region that has been detected.

Another problem is associating the large value of dissipated power with our orbital evolution knowledge. It is obvious that tides are stronger with bodies of higher orbital eccentricity. However, if maintaining the current eccentricity, Enceladus' time-averaged heat production should be about an order of magnitude lesser than we observe: about 1.1 GW. This could be explained by constant heat production of the moon, but only episodic release of power. Or, more like-

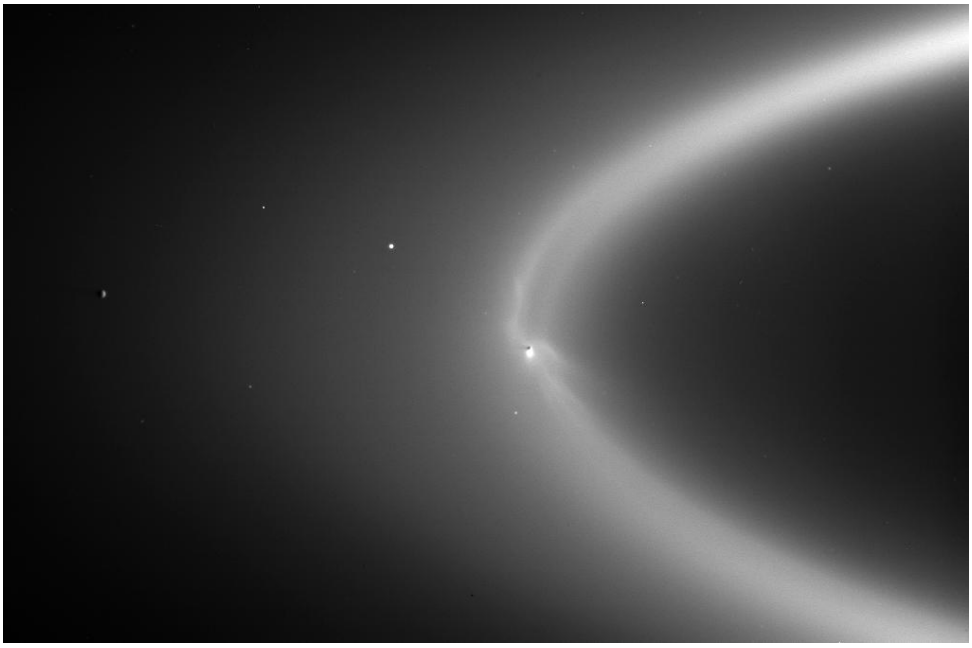

Figure 1.5: In the E ring. Enceladus is shown here in visible light as it orbits in the center of Saturn's E ring that is probably fed by particles ejected from the moon. Almost exactly behind it, occurs the Sun. An interesting feature is the dark gore in the ring's center, probably caused by Enceladus' sweeping effect.

ly, Enceladus may undergo episodes of large heat dissipation, when eccentricity decreases, as well as cold states, when there is no power produced but eccentricity increases. In both cases the time-averaged value of heat production would be much lower than the power released during the episodes. Recently, another possible explanation of the generated heat magnitude emerged, utilizing an exothermic reaction of serpentinization in the silicate core, see e.g. [2].

Perhaps the most interesting and simultaneously most daring question to ask regarding Enceladus is: Is there life? Of the elements essential to life as we know it: carbon, hydrogen, nitrogen, oxygen, sulfur and phosphorus, all but the last one have been found in the moon's plume and it is reasonable to assume that it is also present. Also, the existence of liquid water is highly probable. The sunlight to provide chemical energy would be lacking under the surface, albeit, there have already been found organisms on Earth utilizing other energy sources using mechanisms perhaps available on Enceladus. Far greater problem could pose the cold periods without significant heat dissipation, provided that the hypothesis of episodic heat production proves correct. The question of life remains unanswered so far, however, tiny Enceladus is still one of few places in our Solar System where we are fully legitimate to ask it. Even if it proves to be uninhabited, Enceladus is a wealthy source of information about tidal heating and associated processes. It has shown us that cryovolcanism is real and powerful here and we can relate the obtained knowledge to other icy moons. Therefore, every piece of information regarding it and especially its heat generation mechanisms is well worthy to chase.

Enceladus will remain studied by *Cassini* until the mid-2017, when the spacecraft's fuel runs out. Although it is not quite sure, yet, how the research will continue after the device's demise, the moon has become one of the prime targets for future missions that will, hopefully, provide us with fascinating new data.

2. Mathematical Model

In order to investigate dependence of thermal evolution of Enceladus on various parameters, we developed a mathematical model of the moon and implemented it as a Fortran simulation. Enceladus is considered, here, a continuous body described by Maxwell viscoelasticity so as to compute tidal deformation and dissipation of the satellite's icy shell. We assume purely conductive heat transport and temperature-dependent viscosity and thermal parameters. Radioactive decay is included as an additional heat source in the core. Orbital eccentricity evolution and hydrothermal sources have also been incorporated, in later phase. In this chapter, we provide a detailed description of the equations adopted by our model.

2.1 Deformation of continuum

In our model, we describe the icy mantle of Enceladus as viscoelastic continuum. In order to determine distribution of displacement and stress in the shell, we solve the following equations: The equilibrium equation of a continuum:

$$\nabla \cdot \boldsymbol{\tau} + \vec{f} = 0, \tag{2.1}$$

where $\boldsymbol{\tau}$ is the Cauchy stress tensor and $\vec{f}$ an external volumetric force; the continuity equation for the displacement field $\vec{u}$:

$$\nabla \cdot \vec{u} = 0; \tag{2.2}$$

and finally the rheological equation representing the Maxwell viscoelasticity of the mantle:

$$\boldsymbol{\sigma} - 2\mu\boldsymbol{\epsilon} = -\int_0^t \frac{\mu}{\eta}\boldsymbol{\sigma}\,\mathrm{d}\tau, \tag{2.3}$$

where t is the time, μ, η are the shear modulus and viscosity, respectively. $\boldsymbol{\epsilon}$ is the infinitesimal strain tensor and $\boldsymbol{\sigma}$ the toroidal part of the stress tensor, so called deviator, defined for the symmetric $\boldsymbol{\tau}$ as

$$\boldsymbol{\sigma} = \boldsymbol{\tau} - \frac{1}{3}\left(\operatorname{tr}\boldsymbol{\tau}\right)\boldsymbol{I} = \boldsymbol{\tau} + p\boldsymbol{I}, \tag{2.4}$$

where $\operatorname{tr}\boldsymbol{\tau}$ denotes trace of the second-order tensor $\boldsymbol{\tau}$, $\boldsymbol{I}$ is the unit tensor and p the isotropic pressure. $\boldsymbol{\epsilon}$ can be also expressed as the symmetric traceless part of the displacement gradient.

$$\boldsymbol{\epsilon} = \frac{1}{2}\left(\nabla\vec{u} + (\nabla\vec{u})^{\top}\right). \tag{2.5}$$

We consider the parameters η and μ the functions of temperature at the moment.

Through spectral decomposition into spherical harmonic series (see Appendix), we get

$$\vec{u}(t, r, \vartheta, \varphi) = \sum_{j=0}^{+\infty} \sum_{m=-j}^{j} \sum_{l=j-1}^{j+1} u_{jm}^{l}(t, r)\boldsymbol{Y}_{jm}^{l}(\vartheta, \varphi), \tag{2.6a}$$

$$\vec{f}(t,r,\vartheta,\varphi)=\sum_{j=0}^{+\infty}\sum_{m=-j}^{j}\sum_{l=j-1}^{j+1}f_{jm}^{l}(t,r)\boldsymbol{Y}_{jm}^{l}(\vartheta,\varphi), \tag{2.6b}$$

$$\boldsymbol{\tau}(t,r,\vartheta,\varphi)=\sum_{j=0}^{+\infty}\sum_{m=-j}^{j}\sum_{k=0}^{2}\sum_{l=j-k}^{j+k}\tau_{jm}^{lk}(t,r)\boldsymbol{Y}_{jm}^{lk}(\vartheta,\varphi), \tag{2.6c}$$

$$p(t,r,\vartheta,\varphi)=\sum_{j=0}^{+\infty}\sum_{m=-j}^{j}\tau_{jm}^{j0}(t,r)\boldsymbol{Y}_{jm}^{j0}(\vartheta,\varphi), \tag{2.6d}$$

$$\boldsymbol{\sigma}(t,r,\vartheta,\varphi)=\sum_{j=0}^{+\infty}\sum_{m=-j}^{j}\sum_{n=-1}^{1}\tau_{jm}^{j+2n,2}(t,r)\boldsymbol{Y}_{jm}^{j+2n,2}(\vartheta,\varphi), \tag{2.6e}$$

where u_{jm}^{l}, f_{jm}^{l} and τ_{jm}^{lk} are the proper harmonic coefficients. Provided that μ and η are only radially dependent, we are able to decompose the equations (2.1) - (2.3) spectrally as well and then, due to the orthogonality of the spherical harmonics, solve for each combination of j, m separately. Thus, with the help of the formulas (A.33) - (A.37) and (A.40), we write:

$$\begin{aligned}-f_{jm}^{j-1}(t,r)=&-\sqrt{\frac{j}{3\,(2j+1)}}\left(\frac{\mathrm{d}}{\mathrm{d}r}+\frac{j+1}{r}\right)\tau_{jm}^{j0}(t,r)+\\&+\sqrt{\frac{j-1}{2j-1}}\left(\frac{\mathrm{d}}{\mathrm{d}r}-\frac{j-2}{r}\right)\tau_{jm}^{j-2,2}(t,r)-\\&-\sqrt{\frac{(j+1)\,(2j+3)}{6\,(2j-1)\,(2j+1)}}\left(\frac{\mathrm{d}}{\mathrm{d}r}+\frac{j+1}{r}\right)\tau_{jm}^{j2}(t,r),\end{aligned} \tag{2.7}$$

$$\begin{aligned}-f_{jm}^{j+1}(t,r)=&\sqrt{\frac{j+1}{3\,(2j+1)}}\left(\frac{\mathrm{d}}{\mathrm{d}r}-\frac{j}{r}\right)\tau_{jm}^{j0}(t,r)+\\&+\sqrt{\frac{j\,(2j-1)}{6\,(2j+3)\,(2j+1)}}\left(\frac{\mathrm{d}}{\mathrm{d}r}-\frac{j}{r}\right)\tau_{jm}^{j2}(t,r)-\\&-\sqrt{\frac{j+2}{2j+3}}\left(\frac{\mathrm{d}}{\mathrm{d}r}+\frac{j+3}{r}\right)\tau_{jm}^{j+2,2}(t,r),\end{aligned} \tag{2.8}$$

$$\begin{aligned}0=&\sqrt{\frac{j}{2j+1}}\left(\frac{\mathrm{d}}{\mathrm{d}r}-\frac{j-1}{r}\right)u_{jm}^{j-1}(t,r)-\\&-\sqrt{\frac{j+1}{2j+1}}\left(\frac{\mathrm{d}}{\mathrm{d}r}+\frac{j+2}{r}\right)u_{jm}^{j+1}(t,r),\end{aligned} \tag{2.9}$$

$$\begin{aligned}-\int_0^t\frac{\mu(\tau,r)}{\eta(\tau,r)}\tau_{jm}^{j-2,2}(\tau,r)\,\mathrm{d}\tau=&-2\mu\sqrt{\frac{j-1}{2j-1}}\left(\frac{\mathrm{d}}{\mathrm{d}r}+\frac{j}{r}\right)u_{jm}^{j-1}(t,r)+\\&+\tau_{jm}^{j-2,2}(t,r),\end{aligned} \tag{2.10}$$

$$-\int_0^t \frac{\mu(\tau,r)}{\eta(\tau,r)}\tau_{jm}^{j2}(\tau,r)\,\mathrm{d}\tau = \\ = 2\mu\sqrt{\frac{(j+1)\,(2j+3)}{6\,(2j-1)\,(2j+1)}}\left(\frac{\mathrm{d}}{\mathrm{d}r}-\frac{j-1}{r}\right)u_{jm}^{j-1}(t,r)- \\ -2\mu\sqrt{\frac{j\,(2j-1)}{6\,(2j+3)\,(2j+1)}}\left(\frac{\mathrm{d}}{\mathrm{d}r}+\frac{j+2}{r}\right)u_{jm}^{j+1}(t,r)+ \\ +\tau_{jm}^{j2}(t,r), \tag{2.11}$$

$$-\int_0^t \frac{\mu(\tau,r)}{\eta(\tau,r)}\tau_{jm}^{j+2,2}(\tau,r)\,\mathrm{d}\tau = 2\mu\sqrt{\frac{j+2}{2j+3}}\left(\frac{\mathrm{d}}{\mathrm{d}r}-\frac{j+1}{r}\right)u_{jm}^{j+1}(t,r)+ \\ +\tau_{jm}^{j+2,2}(t,r). \tag{2.12}$$

2.2 Evaluation of gravitational force

The gravitational potential generated by Saturn in a point of the Enceladus' mantle defined by a radial vector in the spherical coordinates $\vec{r}=(r,\vartheta,\varphi)$ in time t is [6]:

$$V=\frac{\omega^2 r^2}{2}\big[1-3\sin^2\vartheta\cos^2\vartheta+ \\ +e\left(3\cos\omega t-9\cos\omega t\sin^2\vartheta\cos^2\varphi-6\sin\omega t\sin^2\vartheta\sin 2\varphi\right)\big], \tag{2.13}$$

where e denotes the eccentricity of the moon's trajectory and $\omega=2\pi/T_p$ is its mean motion, where T_p is the orbital period. For us, however, only the time-variable part V_t of the potential is important [6]:

$$V_\mathrm{t}=\omega^2 r^2 e\left[\frac{3}{2}P_{20}(\cos\vartheta)\cos\omega t- \\ -\frac{1}{4}P_{22}(\cos\vartheta)\left(3\cos\omega t\cos 2\varphi+4\sin\omega t\sin 2\varphi\right)\right], \tag{2.14}$$

where $P_{20}(\cos\theta)$ and $P_{22}(\cos\theta)$ are the associated Legendre polynomials.

This can be rewritten spectrally, using A.1 and A.2 as

$$V_\mathrm{t}=\omega^2 r^2 e\left[\sqrt{\frac{18\pi}{10}}\cos(\omega t)Y_{20}- \\ -\left(\sqrt{\frac{27\pi}{10}}\cos(\omega t)-i\sqrt{\frac{48\pi}{10}}\sin(\omega t)\right)Y_{22}- \\ -\left(\sqrt{\frac{27\pi}{10}}\cos(\omega t)+i\sqrt{\frac{48\pi}{10}}\sin(\omega t)\right)Y_{2,-2}\right]. \tag{2.15}$$

Using the general algebraic properties of the spherical harmonics (A.2) and coefficients (A.7), where the latter is true only if the decomposed function is real (what is our case for V_t), we get

$$(V_\mathrm{t})_{2,-2}Y_{2,-2}+(V_\mathrm{t})_{22}Y_{22}=(V_\mathrm{t})_{22}^{*}Y_{22}^{*}+(V_\mathrm{t})_{22}Y_{22}=2\,\mathrm{Re}\{(V_\mathrm{t})_{22}Y_{22}\}. \tag{2.16}$$

Therefore, we will work only with the non-negative degrees and include only the real part of computed values in the result (however, we will not denote this explicitly in the formulas). We, thus, write

$$V_{\mathrm{t}} = \omega^2 r^2 e \left[\sqrt{\frac{18\pi}{10}} \cos(\omega t) Y_{20} - \right. \\ \left. - 2 \left(\sqrt{\frac{27\pi}{10}} \cos(\omega t) - i \sqrt{\frac{48\pi}{10}} \sin(\omega t) \right) Y_{22} \right] \quad (2.17)$$

and using (A.32) we get the variable component of the gravitational field as

$$\vec{g}_{\mathrm{t}} = -\nabla V_{\mathrm{t}} = -\omega^2 r e \Big[\sqrt{18\pi} \cos(\omega t) \boldsymbol{Y}_{20}^1 - \\ - 2 \left(\sqrt{27\pi} \cos(\omega t) - i \sqrt{48\pi} \sin(\omega t) \right) \boldsymbol{Y}_{22}^1 \Big]. \quad (2.18)$$

The form of the upper allows us to restrict our spectral computations only to the degree $j = 2$ and order $m = 0, 2$. Furthermore, as $\boldsymbol{Y}_{20}^1$, $\boldsymbol{Y}_{20}^3$ and Y_{20} are purely real, we will only take into account the real parts of the coefficients of the order $m = 0$ (however, again, will not denote this explicitly here).

If certain boundary surfaces of a body deform, slight changes occur in the gravitational field acting on its particular elements (so called effect of self-gravity). For our model of Enceladus, such change in the potential can be expressed as [7]

$$(\delta V_{\mathrm{s}})_{jm}(r) = -\frac{4\pi\kappa r}{2j+1} \left(\frac{R_{\mathrm{S}}}{r} \right)^{j+2} (\Delta\rho)_{\mathrm{S}} ((u_r)_{\mathrm{S}})_{jm} \quad (2.19)$$

for the external and

$$(\delta V_{\mathrm{s}})_{jm}(r) = -\frac{4\pi\kappa r}{2j+1} \left(\frac{r}{R} \right)^{j-1} \rho_{\mathrm{ice}} ((u_r)_{\mathrm{R}})_{jm} \quad (2.20)$$

for the internal potential, where R and R_{S} denote the radii of the surface and the silicate core (CMB), respectively and, analogously, the subscripts R and S denote the given property value at the surface and the CMB, respectively, $(u_r)_{jm}$ is the radial component coefficient of the displacement vector, κ is the gravitational constant and $(\Delta\rho)_{\mathrm{S}} = \rho_{\mathrm{water}} - \rho_{\mathrm{ice}}$, where ρ_{water} and ρ_{ice} are the densities of water and ice, respectively.

As the deformation arises only at the degree $j = 2$, we will be specific with respect to this, from now on. For u_r, from (A.27), it holds

$$u_r = \boldsymbol{e}_r \cdot \vec{u} = \left(\sqrt{\frac{2}{5}} u_{20}^1 - \sqrt{\frac{3}{5}} u_{20}^3 \right) Y_{20} + \left(\sqrt{\frac{2}{5}} u_{22}^1 - \sqrt{\frac{3}{5}} u_{22}^3 \right) Y_{22} \quad (2.21)$$

and we can write the whole correction to the potential as

$$\delta V_{\mathrm{s}} = -\frac{4\pi\kappa r}{5} \left(\frac{R_{\mathrm{S}}}{r} \right)^4 (\Delta\rho)_{\mathrm{S}} \left[\left(\sqrt{\frac{2}{5}} (u_{\mathrm{S}})_{20}^1 - \sqrt{\frac{3}{5}} (u_{\mathrm{S}})_{20}^3 \right) Y_{20} + \right. \\ \left. + 2 \left(\sqrt{\frac{2}{5}} (u_{\mathrm{S}})_{22}^1 - \sqrt{\frac{3}{5}} (u_{\mathrm{S}})_{22}^3 \right) Y_{22} \right] -$$

$$- \frac{4\pi\kappa r}{5}\frac{r}{R}\rho_{\mathrm{ice}}\left[\left(\sqrt{\frac{2}{5}}(u_{\mathrm{R}})^1_{20} - \sqrt{\frac{3}{5}}(u_{\mathrm{R}})^3_{20}\right)Y_{20} + \right.$$
$$\left. + 2\left(\sqrt{\frac{2}{5}}(u_{\mathrm{R}})^1_{22} - \sqrt{\frac{3}{5}}(u_{\mathrm{R}})^3_{22}\right)Y_{22}\right], \quad (2.22)$$

where the multiplication of Y_{22} by 2 appeared for the reason of omitting the terms with negative order, again. The correction to the gravitational field will then be

$$\delta\vec{g}_{\mathrm{s}} = -\nabla\delta V_{\mathrm{s}} = 4\pi\kappa\left(\frac{R_{\mathrm{S}}}{r}\right)^4(\Delta\rho)_{\mathrm{S}}\left[\left(\frac{\sqrt{6}}{5}(u_{\mathrm{S}})^1_{20} - \frac{3}{5}(u_{\mathrm{S}})^3_{20}\right)\boldsymbol{Y}^3_{20} + \right.$$
$$\left. + 2\left(\frac{\sqrt{6}}{5}(u_{\mathrm{S}})^1_{22} - \frac{3}{5}(u_{\mathrm{S}})^3_{22}\right)\boldsymbol{Y}^3_{22}\right] +$$
$$+ 4\pi\kappa\frac{r}{R}\rho_{\mathrm{ice}}\left[\left(\frac{2}{5}(u_{\mathrm{R}})^1_{20} - \frac{\sqrt{6}}{5}(u_{\mathrm{R}})^3_{20}\right)\boldsymbol{Y}^1_{20} + \right.$$
$$\left. + 2\left(\frac{2}{5}(u_{\mathrm{R}})^1_{22} - \frac{\sqrt{6}}{5}(u_{\mathrm{R}})^3_{22}\right)\boldsymbol{Y}^1_{22}\right]. \quad (2.23)$$

Finally, we can write, for every point in the mantle, the total variable component of volumetric gravitational force:

$$\vec{f} = \rho_{\mathrm{ice}}(\vec{g}_{\mathrm{t}} + \delta\vec{g}_{\mathrm{s}}) = \left[- \rho_{\mathrm{ice}}\omega^2 re\sqrt{18\pi}\cos\omega t + \right.$$
$$\left. + 4\pi\kappa\rho^2_{\mathrm{ice}}\frac{r}{R}\left(\frac{2}{5}(u_{\mathrm{R}})^1_{20} - \frac{\sqrt{6}}{5}(u_{\mathrm{R}})^3_{20}\right)\right]\boldsymbol{Y}^1_{20} +$$
$$+ 4\pi\kappa\rho_{\mathrm{ice}}\Delta\rho\frac{R^4_{\mathrm{S}}}{r^4}\left(\frac{\sqrt{6}}{5}(u_{\mathrm{S}})^1_{20} - \frac{3}{5}(u_{\mathrm{S}})^3_{20}\right)\boldsymbol{Y}^3_{20} +$$
$$+ 2\left[\rho_{\mathrm{ice}}\omega^2 re\left(\sqrt{27\pi}\cos\omega t - i\sqrt{48\pi}\sin\omega t\right) + \right.$$
$$\left. + 4\pi\kappa\rho^2_{\mathrm{ice}}\frac{r}{R}\left(\frac{2}{5}(u_{\mathrm{R}})^1_{22} - \frac{\sqrt{6}}{5}(u_{\mathrm{R}})^3_{22}\right)\right]\boldsymbol{Y}^1_{22} +$$
$$+ 4\pi\kappa\rho_{\mathrm{ice}}\Delta\rho\frac{R^4_{\mathrm{S}}}{r^4}\left(\frac{\sqrt{6}}{5}(u_{\mathrm{S}})^1_{22} - \frac{3}{5}(u_{\mathrm{S}})^3_{22}\right)\boldsymbol{Y}^3_{22}, \quad (2.24)$$

from where the coefficients f^1_{20}, f^3_{20}, f^1_{22} and f^3_{22} in equations (2.7) and (2.8) are obvious.

2.3 Boundary conditions

On the surface, we use a boundary condition representing its radial deformation:

$$0 = \boldsymbol{\tau}_{\mathrm{R}} \cdot \boldsymbol{e}_r + \rho_{\mathrm{ice}} g_{\mathrm{R}}(u_r)_{\mathrm{R}}\boldsymbol{e}_r, \quad (2.25)$$

where g_{R} is the gravitational intensity at the surface, calculated as

$$g_{\mathrm{R}} = \frac{4}{3}\kappa\pi\frac{(R_{\mathrm{S}}^3\rho_{\mathrm{sil}} + (R^3 - R_{\mathrm{S}}^3)\,\rho_{\mathrm{ice}})}{R^2}. \tag{2.26}$$

After spectral decomposition using (A.26) - (A.31) we get the following two equations for the degree $j = 2$, independently of m:

$$0 = \rho_{\mathrm{ice}} g_{\mathrm{R}} \left(\frac{2}{5}(u_{\mathrm{R}})_{2m}^{1} - \frac{\sqrt{6}}{5}(u_{\mathrm{R}})_{2m}^{3}\right) - \\ - \sqrt{\frac{2}{15}}(\tau_{\mathrm{R}})_{2m}^{20} + \sqrt{\frac{1}{3}}(\tau_{\mathrm{R}})_{2m}^{02} - \sqrt{\frac{7}{30}}(\tau_{\mathrm{R}})_{2m}^{22}, \tag{2.27}$$

$$0 = \rho_{\mathrm{ice}} g_{\mathrm{R}} \left(-\frac{\sqrt{6}}{5}(u_{\mathrm{R}})_{2m}^{1} + \frac{3}{5}(u_{\mathrm{R}})_{2m}^{3}\right) + \\ + \sqrt{\frac{3}{15}}(\tau_{\mathrm{R}})_{2m}^{20} + \sqrt{\frac{1}{35}}(\tau_{\mathrm{R}})_{2m}^{22} - \sqrt{\frac{4}{7}}(\tau_{\mathrm{R}})_{2m}^{42}. \tag{2.28}$$

Boundary condition (so called free-slip) used at the core-mantle boundary represents a layer of water at the CMB. With self-gravity taken into account it has the form of

$$-\boldsymbol{\tau}_{\mathrm{S}} \cdot \boldsymbol{e}_r + \Delta\rho g_{\mathrm{S}}(u_r)_{\mathrm{S}}\boldsymbol{e}_r = -\rho_{\mathrm{water}}(V_{\mathrm{t}} + \delta V_{\mathrm{s}})_{\mathrm{S}}\boldsymbol{e}_r, \tag{2.29}$$

where

$$g_{\mathrm{S}} = \frac{4}{3}\kappa\pi R_{\mathrm{S}}\rho_{\mathrm{sil}} \tag{2.30}$$

is the gravitational intensity at the CMB. Equations (2.29) in the form of spherical coefficients, written for $j = 2$ and $m = 0$ look as follows:

$$\Delta\rho g_{\mathrm{S}} \left(\frac{2}{5}(u_{\mathrm{S}})_{20}^{1} - \frac{\sqrt{6}}{5}(u_{\mathrm{S}})_{20}^{3}\right) + \\ + \sqrt{\frac{2}{15}}(\tau_{\mathrm{S}})_{20}^{20} - \sqrt{\frac{1}{3}}(\tau_{\mathrm{S}})_{20}^{02} + \sqrt{\frac{7}{30}}(\tau_{\mathrm{S}})_{20}^{22} = \\ = -\rho_{\mathrm{water}}\omega^2 R_{\mathrm{S}}^2 e\sqrt{\frac{18\pi}{25}}\cos(\omega t) + \\ + 4\pi\kappa\rho_{\mathrm{water}}\rho_{\mathrm{ice}}\frac{R_{\mathrm{S}}^2}{R}\left(\frac{2}{25}(u_{\mathrm{R}})_{20}^{1} - \frac{\sqrt{6}}{25}(u_{\mathrm{R}})_{20}^{3}\right) + \\ + 4\pi\kappa\rho_{\mathrm{water}}\Delta\rho R_{\mathrm{S}}\left(\frac{2}{25}(u_{\mathrm{S}})_{20}^{1} - \frac{\sqrt{6}}{25}(u_{\mathrm{S}})_{20}^{3}\right), \tag{2.31}$$

$$\Delta\rho g_{\mathrm{S}} \left(-\frac{\sqrt{6}}{5}(u_{\mathrm{S}})_{20}^{1} + \frac{3}{5}(u_{\mathrm{S}})_{20}^{3}\right) - \\ - \sqrt{\frac{3}{15}}(\tau_{\mathrm{S}})_{20}^{20} - \sqrt{\frac{1}{35}}(\tau_{\mathrm{S}})_{20}^{22} + \sqrt{\frac{4}{7}}(\tau_{\mathrm{S}})_{20}^{42} =$$

$$= \rho_{\text{water}}\omega^2 R_{\text{S}}^2 e\sqrt{\frac{27\pi}{25}}\cos(\omega t) -$$
$$- 4\pi\kappa\rho_{\text{water}}\rho_{\text{ice}}\frac{R_{\text{S}}^2}{R}\left(\frac{\sqrt{6}}{25}(u_{\text{R}})_{20}^{1} - \frac{3}{25}(u_{\text{R}})_{20}^{3}\right) -$$
$$- 4\pi\kappa\rho_{\text{water}}\Delta\rho R_{\text{S}}\left(\frac{\sqrt{6}}{25}(u_{\text{S}})_{20}^{1} - \frac{3}{25}(u_{\text{S}})_{20}^{3}\right). \tag{2.32}$$

For $m = 2$ it then holds

$$\Delta\rho g_{\text{S}}\left(\frac{2}{5}(u_{\text{S}})_{22}^{1} - \frac{\sqrt{6}}{5}(u_{\text{S}})_{22}^{3}\right) -$$
$$+ \sqrt{\frac{2}{15}}(\tau_{\text{S}})_{22}^{20} - \sqrt{\frac{1}{3}}(\tau_{\text{S}})_{22}^{02} + \sqrt{\frac{7}{30}}(\tau_{\text{S}})_{22}^{22} =$$
$$= -2\rho_{\text{water}}\omega^2 R_{\text{S}}^2 e\left(-\sqrt{\frac{27\pi}{25}}\cos\omega t + i\sqrt{\frac{48\pi}{25}}\sin\omega t\right) +$$
$$+ 8\pi\kappa\rho_{\text{water}}\rho_{\text{ice}}\frac{R_{\text{S}}^2}{R}\left(\frac{2}{25}(u_{\text{R}})_{22}^{1} - \frac{\sqrt{6}}{25}(u_{\text{R}})_{22}^{3}\right) +$$
$$+ 8\pi\kappa\rho_{\text{water}}\Delta\rho R_{\text{S}}\left(\frac{2}{25}(u_{\text{S}})_{22}^{1} - \frac{\sqrt{6}}{25}(u_{\text{S}})_{22}^{3}\right) \tag{2.33}$$

and

$$\Delta\rho g_{\text{S}}\left(-\frac{\sqrt{6}}{5}(u_{\text{S}})_{22}^{1} + \frac{3}{5}(u_{\text{S}})_{22}^{3}\right) +$$
$$- \sqrt{\frac{3}{15}}(\tau_{\text{S}})_{22}^{20} - \sqrt{\frac{1}{35}}(\tau_{\text{S}})_{22}^{22} + \sqrt{\frac{4}{7}}(\tau_{\text{S}})_{22}^{42} =$$
$$= 2\rho_{\text{water}}\omega^2 R_{\text{S}}^2 e\left(-\sqrt{\frac{81\pi}{50}}\cos\omega t + i\sqrt{\frac{72\pi}{25}}\sin\omega t\right) -$$
$$- 8\pi\kappa\rho_{\text{water}}\rho_{\text{ice}}\frac{R_{\text{S}}^2}{R}\left(\frac{\sqrt{6}}{25}(u_{\text{R}})_{22}^{1} - \frac{3}{25}(u_{\text{R}})_{22}^{3}\right) -$$
$$- 8\pi\kappa\rho_{\text{water}}\Delta\rho R_{\text{S}}\left(\frac{\sqrt{6}}{25}(u_{\text{S}})_{22}^{1} - \frac{3}{25}(u_{\text{S}})_{22}^{3}\right). \tag{2.34}$$

2.4 Heat dissipation and orbital eccentricity evolution

Tidal heat dissipation power is given as

$$H_{\text{TD}} = \frac{\boldsymbol{\sigma} : \boldsymbol{\sigma}}{2\eta}. \tag{2.35}$$

The total dissipated heat in the ice shell in time t can be estimated by

$$H_{\text{TD:tot}}(t) = \int_{R_{\text{S}}}^{R}\sum_{jmkl}\frac{[\sigma_{jm}^{lk}(t,r)]^2}{2\eta(t,r)}r^2\,\mathrm{d}r \tag{2.36}$$

and we define the average total dissipation per orbital period T_p as

$$H_{\mathrm{TD:tot,avg}}(t) = \frac{1}{T_p}\int_{t-T_p}^{t} H_{\mathrm{TD:tot}}(\tau)\,\mathrm{d}\tau. \tag{2.37}$$

We are also able to compute the dissipation locally in any given point as

$$H_{\mathrm{TD:loc}}(t,r,\vartheta,\varphi) = \sum_{i=1}^{3}\sum_{j=1}^{3}\frac{[\sigma_{ij}(t,r,\vartheta,\varphi)]^2}{2\eta(t,r,\vartheta,\varphi)}, \tag{2.38}$$

where σ_{ij} are the Cartesian components of the deviator. The average local periodic dissipation per period is then

$$H_{\mathrm{TD:loc,avg}}(t,r,\vartheta,\varphi) = \frac{1}{T_p}\int_{t-T_p}^{t} H_{\mathrm{TD:loc}}(\tau,r,\vartheta,\varphi)\,\mathrm{d}\tau. \tag{2.39}$$

We can express $H_{\mathrm{TD:loc,avg}}$ spectrally as

$$H_{\mathrm{TD:loc,avg}}(t,r,\vartheta,\varphi) = \sum_{j=0}^{+\infty}\sum_{m=-j}^{j}\left[H_{\mathrm{TD:loc,avg}}\right]_{jm}(t,r)Y_{jm}(\vartheta,\varphi). \tag{2.40}$$

We model the evolution of orbital eccentricity e of Enceladus using the equation encompassing the orbital resonance with Dione [8]:

$$\frac{\mathrm{d}e}{\mathrm{d}t} = \left[\frac{0.49M_{\mathrm{\hbar}}c_{\mathrm{e}}a_{\mathrm{d}}}{M_{\mathrm{d}}aC_{\mathrm{a}}}\right]e^2(1-30.69De^2), \tag{2.41}$$

with

$$D = \left(\frac{R}{R_{\mathrm{\hbar}}}\right)^5\left(\frac{M_{\mathrm{\hbar}}}{M}\right)^2\left(\frac{Q_{\mathrm{\hbar}}}{k_2^{\mathrm{\hbar}}}\right)\left(\frac{k_2}{Q}\right), \tag{2.42}$$

$$\frac{k_2}{Q} = \frac{2}{21}\frac{\kappa}{\omega^5R^5e^2}H_{\mathrm{TD:tot,avg}}, \tag{2.43}$$

$$c_{\mathrm{e}} = \frac{9}{2}\left(\frac{R_{\mathrm{\hbar}}}{a}\right)^5\left(\frac{M}{M_{\mathrm{\hbar}}}\right)^2\omega\frac{k_2^{\mathrm{\hbar}}}{Q_{\mathrm{\hbar}}}, \tag{2.44}$$

$$C_{\mathrm{a}} = 1.19, \tag{2.45}$$

where a is the semi-major axis of Enceladus, $R_{\mathrm{\hbar}}$, $M_{\mathrm{\hbar}}$, $k_2^{\mathrm{\hbar}}$, $Q_{\mathrm{\hbar}}$ are the radius, mass, Love number and dissipation factor of Saturn, respectively, R_{d}, M_{d}, a_{d} are the radius, mass and semi-major axis of Dione, respectively, a is the semi-major axis of Enceladus and M is the mass of Enceladus computed as

$$M = \frac{4}{3}\pi\left[\rho_{\mathrm{sil}}R_{\mathrm{S}}^3 + \rho_{\mathrm{ice}}\left(R^3 - R_{\mathrm{S}}^3\right)\right]. \tag{2.46}$$

2.5 Heat conduction

In our model, we try to determine temperature and heat flow distribution given a heat power source by taking into account conductive heat transport in the form of the heat equation

$$\rho c_p \frac{\partial T}{\partial t} = \nabla \cdot (k \nabla T) + H, \tag{2.47}$$

where T is the absolute temperature, H the volumetric power of the heat source, t time and ρ, c_p and k the density, mass heat capacity at a constant pressure and thermal conductivity, respectively. We can also write

$$\vec{q} = k \nabla T, \tag{2.48}$$

where $-\vec{q}$ represents the heat flux at a given point. We consider the parameters k, ρ and c_p the functions of temperature.

The following spectral decompositions can be written:

$$T(t, r, \vartheta, \varphi) = \sum_{j=0}^{+\infty} \sum_{m=-j}^{j} T_{jm}(t, r) Y_{jm}(\vartheta, \varphi), \tag{2.49a}$$

$$H(t, r, \vartheta, \varphi) = \sum_{j=0}^{+\infty} \sum_{m=-j}^{j} H_{jm}(t, r) Y_{jm}(\vartheta, \varphi), \tag{2.49b}$$

$$\vec{q}(t, r, \vartheta, \varphi) = \sum_{j=0}^{+\infty} \sum_{m=-j}^{j} \sum_{l=j-1}^{j+1} q_{jm}^{l}(t, r) \boldsymbol{Y}_{jm}^{l}(\vartheta, \varphi), \tag{2.49c}$$

where T_{jm}, H_{jm} and q_{jm}^{l} are the corresponding spherical coefficients.

Provided that ρ, c_p and k are only radially dependent, we are able to decompose the equations (2.47) and (2.48) into harmonic series and solve for each combination of j, m separately. Using the relations (A.32) and (A.33), the resulting equations will be as follows:

$$q_{jm}^{j-1}(t, r) = k(t, r) \sqrt{\frac{j}{2j+1}} \left(\frac{\mathrm{d}}{\mathrm{d}r} + \frac{j+1}{r} \right) T_{jm}(t, r), \tag{2.50}$$

$$q_{jm}^{j}(t, r) = 0, \tag{2.51}$$

$$q_{jm}^{j+1}(t, r) = -k(t, r) \sqrt{\frac{j+1}{2j+1}} \left(\frac{\mathrm{d}}{\mathrm{d}r} - \frac{j}{r} \right) T_{jm}(t, r) \tag{2.52}$$

and

$$\rho(t, r) c_p(t, r) \frac{\partial T_{jm}(t, r)}{\partial t} = \sqrt{\frac{j}{2j+1}} \left(\frac{\mathrm{d}}{\mathrm{d}r} - \frac{j-1}{r} \right) q_{jm}^{j-1}(t, r) - \\ - \sqrt{\frac{j+1}{2j+1}} \left(\frac{\mathrm{d}}{\mathrm{d}r} + \frac{j+2}{r} \right) q_{jm}^{j+1}(t, r) + H_{jm}(t, r). \tag{2.53}$$

As a boundary condition on the surface, the constant surface temperature T_{surf} is given. In the center, there holds $T_{00}(r < \alpha) = T_{jm}(r = \alpha)$ for a chosen α depending on numerical discretization and $T_{jm}(r = 0) = 0$ for any $j > 0$.

2.6 Radioactive sources

We include the effect of LLRI (long-lived radioactive isotopes) into the heat source power. These elements occur among the silicates in the core and their volumetric power as a function of time is calculated as

$$H_{\mathrm{RA}}(t) = \rho_{\mathrm{sil}} c_{\mathrm{sil}} \sum_i c_i h_{0i} e^{-\frac{\ln 2}{\tau_i} t}, \tag{2.54}$$

where ρ_{sil} and c_{sil} is the density and concentration of the silicates in the core, respectively, and the sum then counts through all the isotopes known to be present with c_i, h_{0i} and τ_i being the concentration among the silicates, initial power and half-life of the isotope indexed i, respectively.

We assume that the distribution of the radioactive elements in the core is homogeneous, thus its spectral series involves only one term:

$$H_{\mathrm{RA}}(t) = (H_{\mathrm{RA}})_{00}\, Y_{00} = (H_{\mathrm{RA}})_{00}\, \frac{1}{\sqrt{4\pi}}. \tag{2.55}$$

We can also assume another homogeneous, time-independent, hydrothermal source in the core of the total power H_{C}. The total volumetric heat dissipation is thus given as the sum of tidal dissipation in the mantle and the power generated in the core:

$$\begin{aligned} H(t, r, \vartheta, \varphi) = \theta(r - R_{\mathrm{S}}) H_{\mathrm{TD:loc,avg}}(t, r, \vartheta, \varphi) + \\ + \theta(R_{\mathrm{S}} - r) \left[H_{\mathrm{RA}}(t) + \frac{H_{\mathrm{C}}}{\frac{4}{3}\pi R_{\mathrm{S}}^3} \right], \end{aligned} \tag{2.56}$$

where $\theta(x)$ is the Heaviside step function.

3. Numerical Implementation

Our Fortran program (see **Attachment 1**) consists of two main components: a deformational and a conductive unit. A cycle of the program looks as follows: Firstly, viscosity distribution is computed out of given temperatures and passed to the deformational part. Here, tidal heat dissipation in the icy shell is calculated, which is used by the conductive component of the program to obtain new temperature values from which new viscosity distribution in the next cycle will be acquired. Since the timescale of the deformational part computation of one cycle is only of the order of a few orbital periods, the time value is being increased only in the conductive unit.

Here, we provide the discretized form of the used equations as well as a brief overview of the tests used to validate the program.

3.1 Deformational unit

We solve the equations (2.7) - (2.12) for $j = 2$ in each time point $\tilde{t}_\alpha$ using the finite difference method and the radial discretization scheme as shown in figure 3.1: We divide the icy mantle, uniformly, into $V-1$ radially symmetric blocks, bordered by V spherical layers. In between of these layers occur so-called mid-layers. We label the layers and mid-layers by $v = 1, \ldots, V$ and the values of functions defined on them with the appropriate subscript. We denote the distance of the v-th layer from the moon's center r_v and the radial distance between neighboring layers $\Delta r_V = \frac{R-R_S}{V-1}$. $\boldsymbol{\sigma}$, $\boldsymbol{\tau}$, μ and η are assigned to the layers as well as the equations (2.9)-(2.12), while $\vec{u}$, $\vec{f}$ and the equations (2.7) and (2.8) are written to mid-layers.

The scheme near the shell boundaries is illustrated in figure 3.2. It can be seen there that the first 'mid-layer' actually appears slightly over the surface as well as the last one does under the CMB.

The scheme is chosen so that we never derive a function defined on the same (mid-)layer as the equation the derivative is figuring in is. Thus, a value of the radial derivative of a function f on the layer v is computed from its values on the

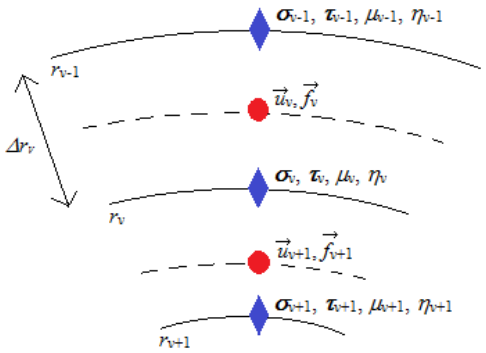

Figure 3.1: Radial discretization scheme of the icy mantle of Enceladus.

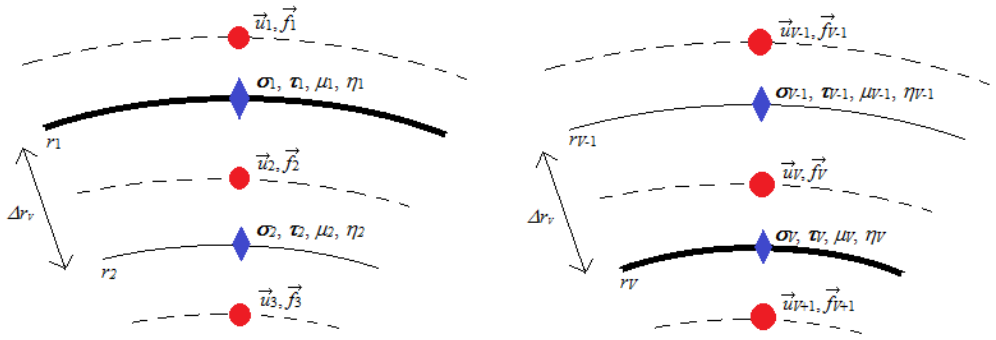

Figure 3.2: Radial discretization scheme near the boundaries (bold lines) of the mantle of Enceladus. The surface is on the left and the CMB on the right.

neighboring mid-layers as

$$\left(\frac{\partial f}{\partial r}\right)\Bigg|_{r=r_v} \approx \frac{f_v - f_{v+1}}{\Delta r_V}. \tag{3.1}$$

The average of function values on neighboring mid-layers is taken whenever the function is not assigned to the same layer v as the equation its value is figuring in:

$$f\left(r_v\right) \approx \frac{f_v + f_{v+1}}{2}, \tag{3.2}$$

and both analogously for a function g on the mid-layer v:

$$\left(\frac{\partial g}{\partial r}\right)\Bigg|_{r=r_v+\frac{\Delta r_V}{2}} \approx \frac{g_{v-1} - g_v}{\Delta r_V}, \tag{3.3}$$

$$g\left(r_v + \frac{\Delta r_V}{2}\right) \approx \frac{g_{v-1} + g_v}{2}. \tag{3.4}$$

For computation of the time integrals we use the trapezoidal rule:

$$\int_0^{\tilde{t}_\alpha} f(\tilde{\tau})\,\mathrm{d}\tilde{\tau} \approx \sum_{\beta=0}^{\alpha-1} \Delta\tilde{t}\left[\frac{f_\beta + f_{\beta+1}}{2}\right], \tag{3.5}$$

where $f_\beta = f(\beta\Delta\tilde{t})$ and $\Delta\tilde{t} = \frac{\tilde{t}_\alpha}{\alpha}$ is the chosen time step value. Of course, we do not know the value of $f_\alpha = f(\tilde{t} = \tilde{t}_\alpha)$, therefore, we have to search for it implicitly. We denote the time $\tilde{t}$, here, with a tilde as this is not the 'real' time t counted. Accounting for $\tilde{t}$ is unnecessary as $\Delta\tilde{t} << \Delta t$. Thus, regarding the character of the problem, we are, without loss of generality, setting $\tilde{t} = 0$, at the beginning of each cycle.

We solve the discretized version of equations (2.7) - (2.12) for $j = 2$ and each m separately. m, here, can take the values $0_r, 2_r, 2_i$ which symbolize the real part of the coefficients of the order 0 and the real and the imaginary parts of the coefficients of the order 2, respectively. On the (mid-)layer v in time t_α the equations look as follows:

$$b_{\alpha,v,m,1} = -\sqrt{\frac{2}{15}}\left(\frac{\left[\tau_{2m}^{2,0}\right]_{\alpha,v-1} - \left[\tau_{2m}^{2,0}\right]_{\alpha,v}}{\Delta r_V} + 3\frac{\left[\tau_{2m}^{2,0}\right]_{\alpha,v-1} + \left[\tau_{2m}^{2,0}\right]_{\alpha,v}}{2r_{v-1} - \Delta r_V}\right) +$$

$$+\sqrt{\frac{1}{3}}\left(\frac{\left[\tau^{0,2}_{2m}\right]_{\alpha,v-1}-\left[\tau^{0,2}_{2m}\right]_{\alpha,v}}{\Delta r_V}-0\frac{\left[\tau^{0,2}_{2m}\right]_{\alpha,v-1}+\left[\tau^{2,2}_{2m}\right]_{\alpha,v}}{2r_{v-1}-\Delta r_V}\right)-$$
$$-\sqrt{\frac{7}{30}}\left(\frac{\left[\tau^{2,2}_{2m}\right]_{\alpha,v-1}-\left[\tau^{2,2}_{2m}\right]_{\alpha,v}}{\Delta r_V}+3\frac{\left[\tau^{2,2}_{2m}\right]_{\alpha,v-1}+\left[\tau^{2,2}_{2m}\right]_{\alpha,v}}{2r_{v-1}-\Delta r_V}\right), \tag{3.6}$$

$$b_{\alpha,v,m,2}=\sqrt{\frac{1}{5}}\left(\frac{\left[\tau^{2,0}_{2m}\right]_{\alpha,v-1}-\left[\tau^{2,0}_{2m}\right]_{\alpha,v}}{\Delta r_V}-2\frac{\left[\tau^{2,0}_{2m}\right]_{\alpha,v-1}+\left[\tau^{2,0}_{2m}\right]_{\alpha,v}}{2r_{v-1}-\Delta r_V}\right)+$$
$$+\sqrt{\frac{1}{35}}\left(\frac{\left[\tau^{2,2}_{2m}\right]_{\alpha,v-1}-\left[\tau^{2,2}_{2m}\right]_{\alpha,v}}{\Delta r_V}-2\frac{\left[\tau^{2,2}_{2m}\right]_{\alpha,v-1}+\left[\tau^{2,2}_{2m}\right]_{\alpha,v}}{2r_{v-1}-\Delta r_V}\right)-$$
$$-\sqrt{\frac{4}{7}}\left(\frac{\left[\tau^{4,2}_{2m}\right]_{\alpha,v-1}-\left[\tau^{4,2}_{2m}\right]_{\alpha,v}}{\Delta r_V}+5\frac{\left[\tau^{4,2}_{2m}\right]_{\alpha,v-1}+\left[\tau^{4,2}_{2m}\right]_{\alpha,v}}{2r_{v-1}-\Delta r_V}\right), \tag{3.7}$$

$$b_{\alpha,v,m,3}=\sqrt{\frac{2}{5}}\left(\frac{[u^1_{2m}]_{\alpha,v}-[u^1_{2m}]_{\alpha,v+1}}{\Delta r_V}-\frac{[u^1_{2m}]_{\alpha,v}+[u^1_{2m}]_{\alpha,v+1}}{2r_v}\right)-$$
$$-\sqrt{\frac{3}{5}}\left(\frac{[u^3_{2m}]_{\alpha,v}-[u^3_{2m}]_{\alpha,v+1}}{\Delta r_V}+4\frac{[u^3_{2m}]_{\alpha,v}+[u^3_{2m}]_{\alpha,v+1}}{2r_v}\right), \tag{3.8}$$

$$b_{\alpha,v,m,4}=-2\mu_v\sqrt{\frac{1}{3}}\left(\frac{[u^1_{2m}]_{\alpha,v}-[u^1_{2m}]_{\alpha,v+1}}{\Delta r_V}+2\frac{[u^1_{2m}]_{\alpha,v}+[u^1_{2m}]_{\alpha,v+1}}{2r_v}\right)+$$
$$+\left(1+\frac{\Delta\tilde{t}}{2}\frac{\mu_v}{\eta_v}\right)\left[\tau^{0,2}_{2m}\right]_{\alpha,v}, \tag{3.9}$$

$$b_{\alpha,v,m,5}=2\mu_v\sqrt{\frac{7}{30}}\left(\frac{[u^1_{2m}]_{\alpha,v}-[u^1_{2m}]_{\alpha,v+1}}{\Delta r_V}-\frac{[u^1_{2m}]_{\alpha,v}+[u^1_{2m}]_{\alpha,v+1}}{2r_v}\right)-$$
$$-2\mu\sqrt{\frac{1}{35}}\left(\frac{[u^3_{2m}]_{\alpha,v}-[u^3_{2m}]_{\alpha,v+1}}{\Delta r_V}+4\frac{[u^3_{2m}]_{\alpha,v}+[u^3_{2m}]_{\alpha,v+1}}{2r_v}\right)+$$
$$+\left(1+\frac{\Delta\tilde{t}}{2}\frac{\mu_v}{\eta_v}\right)\left[\tau^{2,2}_{2m}\right]_{\alpha,v}, \tag{3.10}$$

$$b_{\alpha,v,m,6}=2\mu_v\sqrt{\frac{4}{7}}\left(\frac{[u^3_{2m}]_{\alpha,v}-[u^3_{2m}]_{\alpha,v+1}}{\Delta r_V}-3\frac{[u^3_{2m}]_{\alpha,v}+[u^3_{2m}]_{\alpha,v+1}}{2r_v}\right)+$$
$$+\left(1+\frac{\Delta\tilde{t}}{2}\frac{\mu_v}{\eta_v}\right)\left[\tau^{4,2}_{2m}\right]_{\alpha,v}, \tag{3.11}$$

where the first coefficients on the left are computed from the equation (2.24) using the values obtained in the previous time steps

$$b_{\alpha,v,0_r,1} = \rho_{\text{ice}}\omega^2\left(r_{v-1} - \frac{\Delta r_V}{2}\right)e\sqrt{18\pi}\cos\omega t -$$
$$-4\pi\kappa\rho_{\text{ice}}^2\frac{r_{v-1}-\frac{\Delta r_V}{2}}{R}\left(\frac{2}{5}\frac{\left[u^1_{20_r}\right]_{\alpha-1,1}+\left[u^1_{20_r}\right]_{\alpha-1,2}}{2} - \frac{\sqrt{6}}{5}\frac{\left[u^3_{20_r}\right]_{\alpha-1,1}+\left[u^3_{20_r}\right]_{\alpha-1,2}}{2}\right), \tag{3.12}$$

$$b_{\alpha,v,0_r,2} = -4\pi\kappa\rho_{\text{ice}}\Delta\rho\frac{R_{\text{S}}^4}{\left(r_{v-1}-\frac{\Delta r_V}{2}\right)^4}\times$$
$$\times\left(\frac{\sqrt{6}}{5}\frac{\left[u^2_{20_r}\right]_{\alpha-1,V}+\left[u^1_{20_r}\right]_{\alpha-1,V+1}}{2} - \frac{3}{5}\frac{\left[u^3_{20_r}\right]_{\alpha-1,V}+\left[u^3_{20_r}\right]_{\alpha-1,V+1}}{2}\right), \tag{3.13}$$

$$b_{\alpha,v,2_r,1} = -2\rho_{\text{ice}}\omega^2\left(r_{v-1} - \frac{\Delta r_V}{2}\right)e\sqrt{27\pi}\cos\omega t -$$
$$-8\pi\kappa\rho_{\text{ice}}^2\frac{r_{v-1}-\frac{\Delta r_V}{2}}{R}\left(\frac{2}{5}\frac{\left[u^1_{22_r}\right]_{\alpha-1,1}+\left[u^1_{22_r}\right]_{\alpha-1,2}}{2} - \frac{\sqrt{6}}{5}\frac{\left[u^3_{22_r}\right]_{\alpha-1,1}+\left[u^3_{22_r}\right]_{\alpha-1,2}}{2}\right), \tag{3.14}$$

$$b_{\alpha,v,2_r,2} = -8\pi\kappa\rho_{\text{ice}}\Delta\rho\frac{R_{\text{S}}^4}{\left(r_{v-1}-\frac{\Delta r_V}{2}\right)^4}\times$$
$$\times\left(\frac{\sqrt{6}}{5}\frac{\left[u^2_{22_r}\right]_{\alpha-1,V}+\left[u^1_{22_r}\right]_{\alpha-1,V+1}}{2} - \frac{3}{5}\frac{\left[u^3_{22_r}\right]_{\alpha-1,V}+\left[u^3_{22_r}\right]_{\alpha-1,V+1}}{2}\right), \tag{3.15}$$

$$b_{\alpha,v,2_r,1} = 2\rho_{\text{ice}}\omega^2\left(r_{v-1} - \frac{\Delta r_V}{2}\right)e\sqrt{48\pi}\sin\omega t -$$
$$-8\pi\kappa\rho_{\text{ice}}^2\frac{r_{v-1}-\frac{\Delta r_V}{2}}{R}\left(\frac{2}{5}\frac{\left[u^1_{22_c}\right]_{\alpha-1,1}+\left[u^1_{22_c}\right]_{\alpha-1,2}}{2} - \frac{\sqrt{6}}{5}\frac{\left[u^3_{22_c}\right]_{\alpha-1,1}+\left[u^3_{22_c}\right]_{\alpha-1,2}}{2}\right), \tag{3.16}$$

$$b_{\alpha,v,2_r,2} = -8\pi\kappa\rho_{\text{ice}}\Delta\rho\frac{R_{\text{S}}^4}{\left(r_{v-1}-\frac{\Delta r_V}{2}\right)^4}\times$$
$$\times\left(\frac{\sqrt{6}}{5}\frac{\left[u^1_{22_c}\right]_{\alpha-1,V}+\left[u^1_{22_c}\right]_{\alpha-1,V+1}}{2} - \frac{3}{5}\frac{\left[u^3_{22_c}\right]_{\alpha-1,V}+\left[u^3_{22_c}\right]_{\alpha-1,V+1}}{2}\right) \tag{3.17}$$

and the rest is, for any $m = 0_r, 2_r, 2_c$, obviously:

$$b_{\alpha,v,m,3} = 0, \tag{3.18}$$

$$b_{\alpha,v,m,4} = -\frac{\Delta\tilde{t}}{2}\frac{\mu_v}{\eta_v}\left[\tau^{0,2}_{2m}\right]_{0,v} - \sum_{\beta=1}^{\alpha-1}\Delta\tilde{t}\frac{\mu_v}{\eta_v}\left[\tau^{0,2}_{2m}\right]_{\beta,v}, \tag{3.19}$$

$$b_{\alpha,v,m,5} = -\frac{\Delta\tilde{t}}{2}\frac{\mu_v}{\eta_v}\left[\tau^{2,2}_{2m}\right]_{0,v} - \sum_{\beta=1}^{\alpha-1}\Delta\tilde{t}\frac{\mu_v}{\eta_v}\left[\tau^{2,2}_{2m}\right]_{\beta,v}, \tag{3.20}$$

$$b_{\alpha,v,m,6} = -\frac{\Delta\tilde{t}}{2}\frac{\mu_v}{\eta_v}\left[\tau^{4,2}_{2m}\right]_{0,v} - \sum_{\beta=1}^{\alpha-1}\Delta\tilde{t}\frac{\mu_v}{\eta_v}\left[\tau^{4,2}_{2m}\right]_{\beta,v}. \tag{3.21}$$

Note that the viscosity η_v is constant during one cycle of the unit, however it changes between the cycles according to new temperature calculated in the conductive unit.

Boundary conditions are expressed on the layers $v = 1$ and $v = V$. Surface condition at $v = 1$ substitutes for the equilibrium equations and from (2.27) and (2.28) look as follows:

$$0 = \rho_{\text{ice}} g_R \left(\frac{2}{5}\frac{[u^1_{2m}]_{\alpha,1} + [u^1_{2m}]_{\alpha,2}}{2} - \frac{\sqrt{6}}{5}\frac{[u^3_{2m}]_{\alpha,1} + [u^3_{2m}]_{\alpha,2}}{2}\right) - \\ - \sqrt{\frac{2}{15}}\left[\tau^{2,0}_{2m}\right]_{\alpha,1} + \sqrt{\frac{1}{3}}\left[\tau^{0,2}_{2m}\right]_{\alpha,1} - \sqrt{\frac{7}{30}}\left[\tau^{2,2}_{2m}\right]_{\alpha,1}, \tag{3.22}$$

$$0 = \rho_{\text{ice}} g_R \left(-\frac{\sqrt{6}}{5}\frac{[u^1_{2m}]_{\alpha,1} + [u^1_{2m}]_{\alpha,2}}{2} + \frac{3}{5}\frac{[u^3_{2m}]_{\alpha,1} + [u^3_{2m}]_{\alpha,2}}{2}\right) + \\ + \sqrt{\frac{3}{15}}\left[\tau^{2,0}_{2m}\right]_{\alpha,1} + \sqrt{\frac{1}{35}}\left[\tau^{2,2}_{2m}\right]_{\alpha,1} - \sqrt{\frac{4}{7}}\left[\tau^{4,2}_{2m}\right]_{\alpha,1}. \tag{3.23}$$

The CMB boundary conditions are written in addition to the other equations on the last layer $v = V$ and, from (2.31) - (2.34), the following is true for them:

$$-\rho_{\text{water}}\omega^2 R_{\text{S}}^2 e\sqrt{\frac{18\pi}{25}}\cos(\omega t) + \\ +4\pi\kappa\rho_{\text{water}}\rho_{\text{ice}}\frac{R_{\text{S}}^2}{R}\left(\frac{2}{25}\frac{\left[u^1_{20_r}\right]_{\alpha-1,1} + \left[u^1_{20_r}\right]_{\alpha-1,2}}{2} - \frac{\sqrt{6}}{25}\frac{\left[u^3_{20_r}\right]_{\alpha-1,1} + \left[u^3_{20_r}\right]_{\alpha-1,2}}{2}\right) + \\ +4\pi\kappa\rho_{\text{water}}\Delta\rho R_{\text{S}}\left(\frac{2}{25}\frac{\left[u^1_{20_r}\right]_{\alpha-1,V} + \left[u^1_{20_r}\right]_{\alpha-1,V+1}}{2} - \frac{\sqrt{6}}{25}\frac{\left[u^3_{20_r}\right]_{\alpha-1,V} + \left[u^3_{20_r}\right]_{\alpha-1,V+1}}{2}\right) = \\ = \Delta\rho g_{\text{S}}\left(\frac{2}{5}\frac{\left[u^1_{20_r}\right]_{\alpha,V} + \left[u^1_{20_r}\right]_{\alpha,V+1}}{2} - \frac{\sqrt{6}}{5}\frac{\left[u^3_{20_r}\right]_{\alpha,V} + \left[u^3_{20_r}\right]_{\alpha,V+1}}{2}\right) + \\ + \sqrt{\frac{2}{15}}\left[\tau^{2,0}_{20_r}\right]_{\alpha,V} - \sqrt{\frac{1}{3}}\left[\tau^{0,2}_{20_r}\right]_{\alpha,V} + \sqrt{\frac{7}{30}}\left[\tau^{2,2}_{20_r}\right]_{\alpha,V}, \tag{3.24}$$

$$\rho_{\text{water}}\omega^2 R_{\text{S}}^2 e\sqrt{\frac{27\pi}{25}}\cos(\omega t) - \\ -4\pi\kappa\rho_{\text{water}}\rho_{\text{ice}}\frac{R_{\text{S}}^2}{R}\left(\frac{\sqrt{6}}{25}\frac{\left[u^1_{20_r}\right]_{\alpha-1,1} + \left[u^1_{20_r}\right]_{\alpha-1,2}}{2} - \frac{3}{25}\frac{\left[u^3_{20_r}\right]_{\alpha-1,1} + \left[u^3_{20_r}\right]_{\alpha-1,2}}{2}\right) - \\ -4\pi\kappa\rho_{\text{water}}\Delta\rho R_{\text{S}}\left(\frac{\sqrt{6}}{25}\frac{\left[u^1_{20_r}\right]_{\alpha-1,V} + \left[u^1_{20_r}\right]_{\alpha-1,V+1}}{2} - \frac{3}{25}\frac{\left[u^3_{20_r}\right]_{\alpha-1,V} + \left[u^3_{20_r}\right]_{\alpha-1,V+1}}{2}\right) =$$

$$= \Delta\rho g_{\mathrm{S}} \left(-\frac{\sqrt{6}}{5} \frac{\left[u^1_{20_r}\right]_{\alpha,1} + \left[u^1_{20_r}\right]_{\alpha,V+1}}{2} + \frac{3}{5} \frac{\left[u^3_{20_r}\right]_{\alpha,1} + \left[u^3_{20_r}\right]_{\alpha,2}}{2} \right) -$$
$$- \sqrt{\frac{3}{15}} \left[\tau^{2,0}_{20_r}\right]_{\alpha,V} - \sqrt{\frac{1}{35}} \left[\tau^{2,2}_{20_r}\right]_{\alpha,V} + \sqrt{\frac{4}{7}} \left[\tau^{4,2}_{20_r}\right]_{\alpha,V}, \quad (3.25)$$

$$2\rho_{\mathrm{water}}\omega^2 R_{\mathrm{S}}^2 e \sqrt{\frac{27\pi}{25}} \cos(\omega t) +$$
$$+8\pi\kappa\rho_{\mathrm{water}}\rho_{\mathrm{ice}} \frac{R_{\mathrm{S}}^2}{R} \left(\frac{2}{25} \frac{\left[u^1_{22_r}\right]_{\alpha-1,1} + \left[u^1_{22_r}\right]_{\alpha-1,2}}{2} - \frac{\sqrt{6}}{25} \frac{\left[u^3_{22_r}\right]_{\alpha-1,1} + \left[u^3_{22_r}\right]_{\alpha-1,2}}{2} \right) +$$
$$+8\pi\kappa\rho_{\mathrm{water}}\Delta\rho R_{\mathrm{S}} \left(\frac{2}{25} \frac{\left[u^1_{22_r}\right]_{\alpha-1,V} + \left[u^1_{22_r}\right]_{\alpha-1,V+1}}{2} - \frac{\sqrt{6}}{25} \frac{\left[u^3_{22_r}\right]_{\alpha-1,V} + \left[u^3_{22_r}\right]_{\alpha-1,V+1}}{2} \right) =$$
$$= \Delta\rho g_{\mathrm{S}} \left(\frac{2}{5} \frac{\left[u^1_{22_r}\right]_{\alpha,V} + \left[u^1_{22_r}\right]_{\alpha,V+1}}{2} - \frac{\sqrt{6}}{5} \frac{\left[u^3_{22_r}\right]_{\alpha,V} + \left[u^3_{22_r}\right]_{\alpha,V+1}}{2} \right) +$$
$$+ \sqrt{\frac{2}{15}} \left[\tau^{2,0}_{22_r}\right]_{\alpha,V} - \sqrt{\frac{1}{3}} \left[\tau^{0,2}_{22_r}\right]_{\alpha,V} + \sqrt{\frac{7}{30}} \left[\tau^{2,2}_{22_r}\right]_{\alpha,V}, \quad (3.26)$$

$$- 2\rho_{\mathrm{water}}\omega^2 R_{\mathrm{S}}^2 e \sqrt{\frac{81\pi}{50}} \cos(\omega t) -$$
$$-8\pi\kappa\rho_{\mathrm{water}}\rho_{\mathrm{ice}} \frac{R_{\mathrm{S}}^2}{R} \left(\frac{\sqrt{6}}{25} \frac{\left[u^1_{22_r}\right]_{\alpha-1,1} + \left[u^1_{22_r}\right]_{\alpha-1,2}}{2} - \frac{3}{25} \frac{\left[u^3_{22_r}\right]_{\alpha-1,1} + \left[u^3_{22_r}\right]_{\alpha-1,2}}{2} \right) -$$
$$-8\pi\kappa\rho_{\mathrm{water}}\Delta\rho R_{\mathrm{S}} \left(\frac{\sqrt{6}}{25} \frac{\left[u^1_{22_r}\right]_{\alpha-1,V} + \left[u^1_{22_r}\right]_{\alpha-1,V+1}}{2} - \frac{3}{25} \frac{\left[u^3_{22_r}\right]_{\alpha-1,V} + \left[u^3_{22_r}\right]_{\alpha-1,V+1}}{2} \right) =$$
$$= \Delta\rho g_{\mathrm{S}} \left(-\frac{\sqrt{6}}{5} \frac{\left[u^1_{22_r}\right]_{\alpha,1} + \left[u^1_{22_r}\right]_{\alpha,V+1}}{2} + \frac{3}{5} \frac{\left[u^3_{22_r}\right]_{\alpha,1} + \left[u^3_{22_r}\right]_{\alpha,2}}{2} \right) -$$
$$- \sqrt{\frac{3}{15}} \left[\tau^{2,0}_{22_r}\right]_{\alpha,V} - \sqrt{\frac{1}{35}} \left[\tau^{2,2}_{22_r}\right]_{\alpha,V} + \sqrt{\frac{4}{7}} \left[\tau^{4,2}_{22_r}\right]_{\alpha,V}, \quad (3.27)$$

$$- 2\rho_{\mathrm{water}}\omega^2 R_{\mathrm{S}}^2 e \sqrt{\frac{48\pi}{50}} \sin(\omega t) +$$
$$+8\pi\kappa\rho_{\mathrm{water}}\rho_{\mathrm{ice}} \frac{R_{\mathrm{S}}^2}{R} \left(\frac{2}{25} \frac{\left[u^1_{22_c}\right]_{\alpha-1,1} + \left[u^1_{22_c}\right]_{\alpha-1,2}}{2} - \frac{\sqrt{6}}{25} \frac{\left[u^3_{22_c}\right]_{\alpha-1,1} + \left[u^3_{22_c}\right]_{\alpha-1,2}}{2} \right) +$$
$$+8\pi\kappa\rho_{\mathrm{water}}\Delta\rho R_{\mathrm{S}} \left(\frac{2}{25} \frac{\left[u^1_{22_c}\right]_{\alpha-1,V} + \left[u^1_{22_c}\right]_{\alpha-1,V+1}}{2} - \frac{\sqrt{6}}{25} \frac{\left[u^3_{22_c}\right]_{\alpha-1,V} + \left[u^3_{22_c}\right]_{\alpha-1,V+1}}{2} \right) =$$
$$= \Delta\rho g_{\mathrm{S}} \left(\frac{2}{5} \frac{\left[u^1_{22_c}\right]_{\alpha,V} + \left[u^1_{22_c}\right]_{\alpha,V+1}}{2} - \frac{\sqrt{6}}{5} \frac{\left[u^3_{22_c}\right]_{\alpha,V} + \left[u^3_{22_c}\right]_{\alpha,V+1}}{2} \right) +$$
$$+ \sqrt{\frac{2}{15}} \left[\tau^{2,0}_{22_c}\right]_{\alpha,V} - \sqrt{\frac{1}{3}} \left[\tau^{0,2}_{22_c}\right]_{\alpha,V} + \sqrt{\frac{7}{30}} \left[\tau^{2,2}_{22_c}\right]_{\alpha,V}, \quad (3.28)$$

$$
\begin{aligned}
&2\rho_{\mathrm{water}}\omega^2 R_{\mathrm{S}}^2 e\sqrt{\frac{72\pi}{25}}\sin(\omega t)- \\
&-8\pi\kappa\rho_{\mathrm{water}}\rho_{\mathrm{ice}}\frac{R_{\mathrm{S}}^2}{R}\left(\frac{\sqrt{6}}{25}\frac{\left[u^1_{22_c}\right]_{\alpha-1,1}+\left[u^1_{22_c}\right]_{\alpha-1,2}}{2}-\frac{3}{25}\frac{\left[u^3_{22_c}\right]_{\alpha-1,1}+\left[u^3_{22_c}\right]_{\alpha-1,2}}{2}\right)- \\
&-8\pi\kappa\rho_{\mathrm{water}}\Delta\rho R_{\mathrm{S}}\left(\frac{\sqrt{6}}{25}\frac{\left[u^1_{22_c}\right]_{\alpha-1,V}+\left[u^1_{22_c}\right]_{\alpha-1,V+1}}{2}-\frac{3}{25}\frac{\left[u^3_{22_c}\right]_{\alpha-1,V}+\left[u^3_{22_c}\right]_{\alpha-1,V+1}}{2}\right)= \\
&\qquad=\Delta\rho g_{\mathrm{S}}\left(-\frac{\sqrt{6}}{5}\frac{\left[u^1_{22_c}\right]_{\alpha,1}+\left[u^1_{22_c}\right]_{\alpha,V+1}}{2}+\frac{3}{5}\frac{\left[u^3_{22_c}\right]_{\alpha,1}+\left[u^3_{22_c}\right]_{\alpha,2}}{2}\right)- \\
&\qquad\qquad-\sqrt{\frac{3}{15}}\left[\tau^{2,0}_{22_c}\right]_{\alpha,V}-\sqrt{\frac{1}{35}}\left[\tau^{2,2}_{22_c}\right]_{\alpha,V}+\sqrt{\frac{4}{7}}\left[\tau^{4,2}_{22_c}\right]_{\alpha,V}, \quad (3.29)
\end{aligned}
$$

All the equations above compose a system of $6V+2$ linear algebraic equations for each combination of j and m, and the problem can be written in the form of a band matrix. We solve the problem using the Fortran subroutines *bandec* and *banbks* of Numerical Recipes.

After solving the equations for time $\tilde{t}_\alpha$, we compute the total dissipated power from (2.36) using the trapezoidal rule, again:

$$
[H_{\mathrm{TD:tot}}]_\alpha=\sum_{i=1}^{V-1}\sum_{jmkl}\frac{1}{2}\left[\frac{\left([\sigma^{lk}_{jm}]_{\alpha,i}\right)^2}{2\eta_{\alpha,i}}r_i^2+\frac{\left([\sigma^{lk}_{jm}]_{\alpha,i+1}\right)^2}{2\eta_{\alpha,i+1}}r_{i+1}^2\right]\Delta r_V \qquad (3.30)
$$

and similarly the average total power from (2.37):

$$
H_{\mathrm{TD:tot,avg}}(t)=\frac{1}{2T_p}\sum_{\beta=\alpha-\frac{T_p}{\Delta\tilde{t}}}^{\alpha-1}\left([H_{\mathrm{TD:tot}}]_\beta+[H_{\mathrm{TD:tot}}]_{\beta+1}\right)\Delta\tilde{t}. \qquad (3.31)
$$

If the condition for sufficiently small average periodic dissipation change

$$
2\frac{|H_{\mathrm{TD:tot,avg}}(t_\alpha)-H_{\mathrm{TD:tot,avg}}(t_{\alpha-1})|}{H_{\mathrm{TD:tot,avg}}(t_\alpha)+H_{\mathrm{TD:tot,avg}}(t_{\alpha-1})}<\epsilon, \qquad (3.32)
$$

where ϵ is a certain small number, is met, we start to calculate the dissipation locally, using the Cartesian representation of the deviator:

$$
[H_{\mathrm{TD:loc}}]_{\alpha,v,\theta,\phi}=\sum_{i=1}^{3}\sum_{j=1}^{3}\frac{\left([\sigma_{ij}]_{\alpha,v,\theta,\phi}\right)^2}{2\eta_{\alpha,v,\theta,\phi}}, \qquad (3.33)
$$

where the subscripts v,θ,ϕ denote the function expressed on the discrete point on the layer v, characterized by the discretized values θ,ϕ of the angular variables ϑ,φ, respectively. To obtain the Cartesian coefficients, we perform spherical analysis by means of the equations (A.45) - (A.50). In the whole program, we compute the Clebsch-Gordan coefficients and associated Legendre polynomials using the programs *cw* and *dpnm*, respectively, developed at the Department of Geophysics. Here, we use 3D variable viscosity values $\eta_{\alpha,v,\theta,\phi}$, in contrast to to the previous equations, where the character of the problem allowed us to only

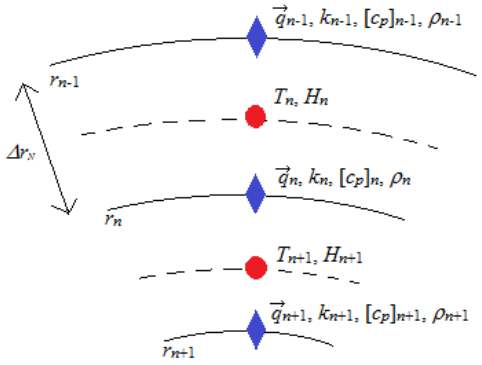

Figure 3.3: Radial discretization scheme of the body of Enceladus.

use the layer-averaged values. Finally, we calculate the average local dissipation distribution

$$[H_{\text{TD:loc,avg}}]_{\alpha,v,\theta,\phi} = \frac{1}{2T_p} \sum_{\beta=\alpha-\frac{T_p}{\Delta\tilde{t}}}^{\alpha-1} \left([H_{\text{TD:loc}}]_{\beta,v,\theta,\phi} + [H_{\text{TD:loc}}]_{\beta+1,v,\theta,\phi}\right) \Delta\tilde{t} \tag{3.34}$$

and write it in the form of a spectral series using the trapezoidal approximation of (A.6) up to the degree $j = 2$. Moreover, only the coefficients of $jm = 00, 20, 22$ are nonzero. The series representation is then passed to the conductive unit.

3.2 Conductive unit

We solve the heat equation (2.47) for $jm = 00, 20, 22$ using the finite difference method on the radial scheme as shown in figure 3.3: We divide the body of Enceladus uniformly into $N - 1/2$ radially symmetric blocks bordered by $N - 1$ spherical layers. Exactly between every two layers, we put a mid-layer. The half-block encircles the center of the moon, where also the last mid-layer is placed. We label the layers and mid-layers by $n = 1, \ldots, N$ and the values of functions defined on them with the appropriate subscript, the distance of the n-th layer from the moon's center r_n and $\Delta r_N = \frac{R}{N-3/2}$ the radial distance between neighboring layers. $\vec{q}$, k, ρ and c_p and the equations (2.50) and (2.52) are assigned for the layers while T, H and (2.53) are written on the mid-layers. Analogously to (3.1) - (3.4), the radial derivative of each function is computed from its values on the neighboring layers and the average of those is taken whenever the function is not defined on the same layer as the equation it is figuring in.

The scheme near the surface and the center of the moon is depicted in figure 3.4. Similarly to the previous case, the first 'mid-layer' is placed a bit over the surface. However, the last layer has now a number $V - 1$ and the center of the body serves as the V-th mid-layer.

The time integration in time t_α is performed by the means of the Crank-Nicholson method:

$$\rho c_p \frac{T_\alpha - T_{\alpha-1}}{\Delta t} = \frac{1}{2}\left(\nabla \cdot q_\alpha + \nabla \cdot q_{\alpha-1}\right) + \frac{1}{2}\left(H_\alpha + H_{\alpha-1}\right), \tag{3.35}$$

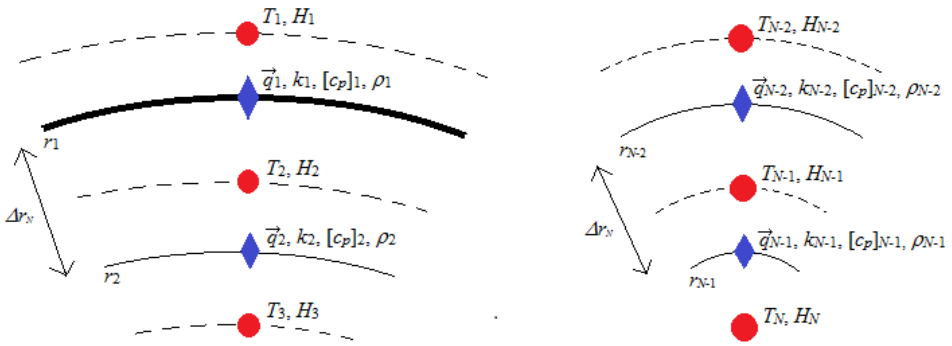

Figure 3.4: Radial discretization scheme near the surface (bold line on the left) and the center (red point on the right) of the body of Enceladus.

where Δt is the chosen time step value. The discretized equations (2.50), (2.52) and (2.53) for the layer n in time t_α look as follows:

$$0 = -\left[q_{jm}^{j-1}\right]_{\alpha,n} + k_{\alpha,n}\sqrt{\frac{j}{2j+1}}\times \\ \times\left(\frac{[T_{jm}]_{\alpha,n}-[T_{jm}]_{\alpha,n+1}}{\Delta r_N}+(j+1)\frac{[T_{jm}]_{\alpha,n}+[T_{jm}]_{\alpha,n+1}}{2r_n}\right), \quad (3.36)$$

$$0 = -\left[q_{jm}^{j+1}\right]_{\alpha,n} - k_{\alpha,n}\sqrt{\frac{j+1}{2j+1}}\times \\ \times\left(\frac{[T_{jm}]_{\alpha,n}-[T_{jm}]_{\alpha,n+1}}{\Delta r_N}-j\frac{[T_{jm}]_{\alpha,n}+[T_{jm}]_{\alpha,n+1}}{2r_n}\right), \quad (3.37)$$

$$\frac{1}{2}\sqrt{\frac{j+1}{2j+1}}\left(\frac{\left[q_{jm}^{j+1}\right]_{\alpha-1,n-1}-\left[q_{jm}^{j+1}\right]_{\alpha-1,n}}{\Delta r_N}+(j+2)\frac{\left[q_{jm}^{j+1}\right]_{\alpha-1,n-1}+\left[q_{jm}^{j+1}\right]_{\alpha-1,n}}{2r_{n-1}-\Delta r_N}\right)- \\ -\frac{1}{2}\sqrt{\frac{j}{2j+1}}\left(\frac{\left[q_{jm}^{j-1}\right]_{\alpha-1,n-1}-\left[q_{jm}^{j-1}\right]_{\alpha-1,n}}{\Delta r_N}-(j-1)\frac{\left[q_{jm}^{j-1}\right]_{\alpha-1,n-1}+\left[q_{jm}^{j-1}\right]_{\alpha-1,n}}{2r_{n-1}-\Delta r_N}\right)- \\ -\frac{1}{2}[H_{jm}]_{\alpha-1,n}-\rho_n\frac{[c_p]_{\alpha,n}+[c_p]_{\alpha-1,n}}{2}\frac{[T_{jm}]_{\alpha-1,n}}{\Delta t}-= \\ =-\rho_n\frac{[c_p]_{\alpha,n}+[c_p]_{\alpha-1,n}}{2}\frac{[T_{jm}]_{\alpha,n}}{\Delta t}+\frac{1}{2}[H_{jm}]_{\alpha,n}+ \\ +\frac{1}{2}\sqrt{\frac{j}{2j+1}}\left(\frac{\left[q_{jm}^{j-1}\right]_{\alpha,n-1}-\left[q_{jm}^{j-1}\right]_{\alpha,n}}{\Delta r_N}-(j-1)\frac{\left[q_{jm}^{j-1}\right]_{\alpha,n-1}+\left[q_{jm}^{j-1}\right]_{\alpha,n}}{2r_{n-1}-\Delta r_N}\right)- \\ -\frac{1}{2}\sqrt{\frac{j+1}{2j+1}}\left(\frac{\left[q_{jm}^{j+1}\right]_{\alpha,n-1}-\left[q_{jm}^{j+1}\right]_{\alpha,n}}{\Delta r_N}+(j+2)\frac{\left[q_{jm}^{j+1}\right]_{\alpha,n-1}+\left[q_{jm}^{j+1}\right]_{\alpha,n}}{2r_{n-1}-\Delta r_N}\right), \quad (3.38)$$

where $[c_p]_{\alpha,n}$ and $k_{\alpha,n}$ are calculated from the temperatures obtained in the previous time step and ρ_n remains constant. As a surface boundary condition, constant homogeneous surface temperature $[T_{00}]_{\alpha,1} = \text{const.}$, $[T_{jm}]_{\alpha,1} = 0$, for $j \neq 0$, is given. At the core, we use, for $j = 0$, $[T_{jm}]_{\alpha,N} = [T_{jm}]_{\alpha,N-1}$ and, for $j > 0$, $[T_{jm}]_{\alpha,N} = 0$.

The equations above form a set of $3N - 2$ linear algebraic equations, which can be represented by a band matrix, and which we solve using the Fortran subroutines *bandec* and *banbks* of Numerical Recipes, again.

The unit terminates if the temperature change is too big in any point:

$$\frac{|T_{\alpha,n,\theta,\phi} - T_{\gamma,n,\theta,\phi}|}{T_{\gamma,n,\theta,\phi}} > \delta, \tag{3.39}$$

where γ denotes the time when the last heat dissipation update occurred and δ is a certain, rather small, value. In that case, new viscosity distribution is computed as an exponential function of T_α and the program passes to the deformational part. If, in any point, temperature $T_1 > 273\,\mathrm{K}$ occurs, we do not further increase the viscosity: $\eta(T_1) = \eta(273\,\mathrm{K})$. Of course, since the radial discretization of the two units is different, we have to linearly interpolate the temperature and heat source values, whenever transitioning between them.

3.3 Orbital eccentricity evolution

We solve the orbital eccentricity evolution equation, in the time t_α, using a semi-implicit method of the form:

$$\frac{e_\alpha - e_{\alpha-1}}{\Delta t} = A e_\alpha e_{\alpha-1} B, \tag{3.40}$$

where

$$A = \left[\frac{0.49 M_{\text{ somethingwrong}} c_\mathrm{e} a_\mathrm{d}}{M_\mathrm{d} a C_\mathrm{a}}\right] \tag{3.41}$$

and

$$B = 1 - 30.69 De^2. \tag{3.42}$$

This leads to the following expression of e_α:

$$e_\alpha = \frac{e_{\alpha-1}}{1 - AB\Delta t e_{\alpha-1}}. \tag{3.43}$$

We calculate eccentricity evolution in the conductive unit, using, for greater precision, average tidal power that was at first evaluated locally and then integrated through the whole body. We add another terminating condition there, for too large eccentricity changes:

$$\frac{|e_\alpha - e_\gamma|}{e_\gamma} > \delta_e, \tag{3.44}$$

where γ denotes the time when the last heat dissipation update occurred and δ_e is a small number.

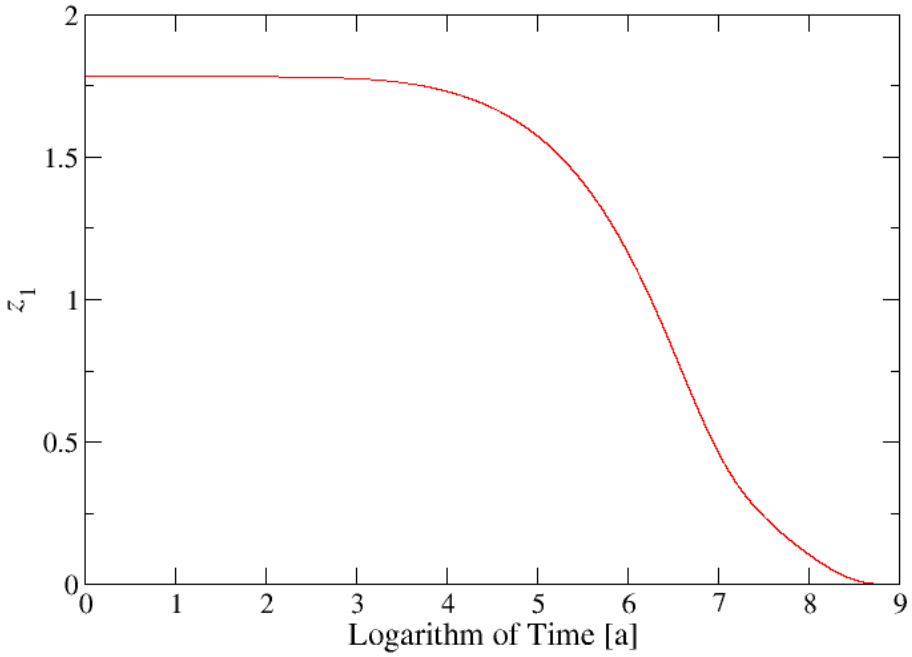

Figure 3.5: Conductive unit test for $j = 0$.

3.4 Program tests

The deformational part has been tested against a similar program developed by O. Čadek.

The conductive part has been tested, for $j = 0$, using the energy conservation law: With constant heat sources and other physical parameters, after some time, the system should proceed to a steady state, when the heat generation is equal to the heat flux through the surface:

$$0 = \int_V H(r, \vartheta, \varphi)\,\mathrm{d}V + \int_{\text{Surface}} \vec{q}(\vartheta, \varphi) \cdot \mathrm{d}\vec{S}. \tag{3.45}$$

Let us define

$$z_1 = 2\frac{|\int_V H(r, \vartheta, \varphi)\,\mathrm{d}V + \int_{\text{Surface}} \vec{q}(\vartheta, \varphi) \cdot \mathrm{d}\vec{S}|}{|\int_V H(r, \vartheta, \varphi)\,\mathrm{d}V| + |\int_{\text{Surface}} \vec{q}(\vartheta, \varphi) \cdot \mathrm{d}\vec{S}|}, \tag{3.46}$$

what represents the relative value of the deviation of the left hand side of (3.45) from zero, in regard of the mean of the sum of the absolute values of energy input and output. In the test, we watched the convergence of z_1 to zero, which is demonstrated in figure 3.5 for time step $\Delta t = 100\,\mathrm{a}$, however tests with different time steps, up to 5000 a, accounted for the same behavior.

For $j > 0$, we used the fact that the steady state should be described by the solution of the Poisson equation in the form:

$$\nabla^2 T(r, \vartheta, \varphi) = -\frac{H(r, \vartheta, \varphi)}{k}. \tag{3.47}$$

The solution of (3.47) can be written for each j and m separately (see [9]):

$$\tilde{T}_{jm}(r) = \frac{1}{k(2j+1)r^{j+1}} I^1_{jm}(r) + \frac{r^j}{k(2j+1)} I^2_{jm}(r) + A_{jm} r^j + B_{jm} \frac{1}{r^{j+1}}, \quad (3.48)$$

where A_{jm} and B_{jm} are certain constants and

$$I^1_{jm}(r) = \int_0^r (r')^{j+2} H_{jm}(r') dr' \quad (3.49)$$

and

$$I^2_{jm}(r) = \int_r^R (r')^{-j+1} H_{jm}(r') dr'. \quad (3.50)$$

We determine the constants from the boundary conditions:

$$B_{jm} = 0, \quad (3.51)$$

$$A_{jm} = -\frac{I^1_{jm}(R)}{k(2j+1)R^{2j+1}}. \quad (3.52)$$

For chosen j, m and v we integrate $\tilde{T}_{22}(r_v)$ numerically and define the relative deviation from the proper solution as

$$z_2 = 2\frac{|\tilde{T}_{jm}(r_v) - (T_{jm})_v|}{|\tilde{T}_{jm}(r_v)| + |(T_{jm})_v|}. \quad (3.53)$$

The progression of $\mathrm{Re}\{z_2\}$ towards zero, for $j = 2$ and $m = 2$ coefficient and a $H_{22} = \text{const}$ in the whole body, is shown in figure 3.6 for $\Delta t = 5000$a. For other values of Δt as well as for $\mathrm{Im}\{z_2\}$, the graph behaves equally.

The orbital eccentricity evolution test has been performed against the analytical solution of

$$\frac{\mathrm{d}e}{\mathrm{d}t} = Ke^2, \quad (3.54)$$

where $K = \text{const.}$, for time-independent tidal heating. The solution $e = e(t)$ has a form:

$$e(t) = \frac{\tilde{e}_0}{1 - Kt\tilde{e}_0}, \quad (3.55)$$

where $\tilde{e}_0 = e(0)$. Figures 3.7 and 3.8 show the plot of analytical and numerical solution for negative and positive K, respectively. Both solutions agree excellently.

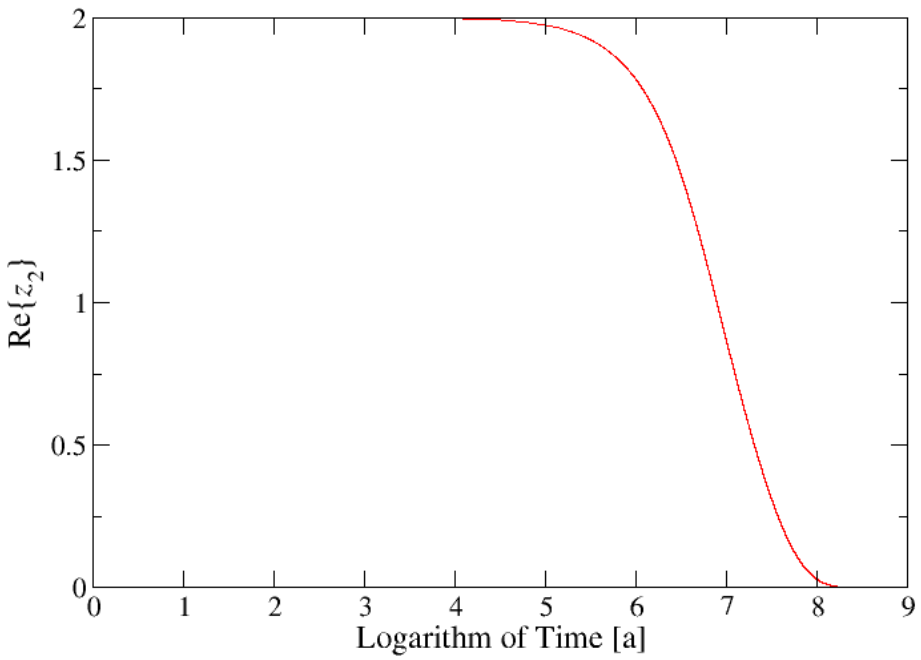

Figure 3.6: Conductive unit test for $j = 2$, $m = 2$.

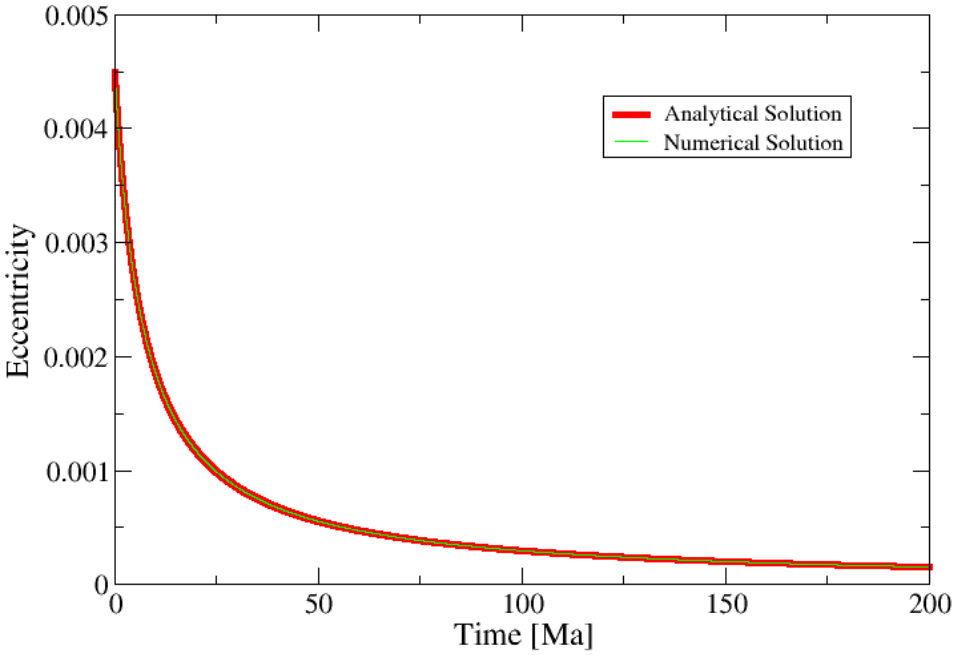

Figure 3.7: Test of eccentricity evolution equation solution for $K < 0$.

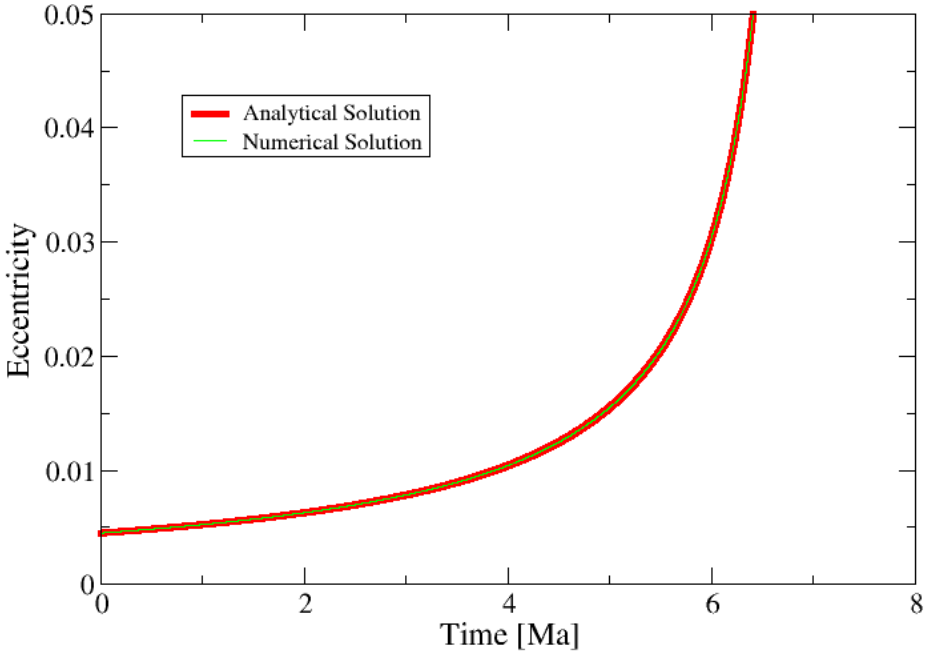

Figure 3.8: Test of eccentricity evolution equation solution for $K > 0$.

4. Results

For all of our computations we use the physical parameters as stated in Table 4.1, where the temperature dependence of $c_{p\,\mathrm{ice}}$ and k_{ice} is according to [10]. We define the viscosity as an exponential function of temperature

$$\eta(T) = Ae^{-BT}, \tag{4.1}$$

satisfying that the maximum viscosity $\eta(90\,\mathrm{K}) = 10^{18}\,\mathrm{Pa\,s}$. For various minimal viscosity values $\eta_{\mathrm{min}} = \eta(273\,\mathrm{K})$ we get the coefficients A and B as in Table 4.2. LLRI sources are characterized by the parameters in Table 4.3, according to [11].

Radius of Enceladus	R	252000	km
Radius of the silicate core	R_{S}	172000	km
Radius of the icy mantle	R_{ice}	80000	km
Water ice density	ρ_{ice}	940	$\mathrm{kg\,m^{-3}}$
Water density	ρ_{water}	1000	$\mathrm{kg\,m^{-3}}$
Silicate density	ρ_{sil}	3000	$\mathrm{kg\,m^{-3}}$
Current eccentricity	e_0	0.0045	
Orbital period	T_p	1.37	day
Shear modulus of the ice shell	μ_{ice}	3.3×10^9	Pa
Surface temperature	T_{surf}	90	K
Water ice isobaric mass heat capacity	$c_{p\,\mathrm{ice}}(T)$	$185 + 7.037T$	$\mathrm{J\,kg^{-1}\,K^{-1}}$
Silicate isobaric mass heat capacity	$c_{p\,\mathrm{sil}}$	920	$\mathrm{J\,kg^{-1}\,K^{-1}}$
Water ice thermal conductivity	$k_{\mathrm{ice}}(T)$	$0.4685 + \frac{488.12}{T}$	$\mathrm{W\,m^{-1}\,K^{-1}}$
Silicate thermal conductivity	k_{sil}	4.2	$\mathrm{W\,m^{-1}\,K^{-1}}$
Concentration of silicates in the core	c_{sil}	100	%

Table 4.1: Used model parameters.

$\eta_{\mathrm{min}}\,[10^{13}\,\mathrm{Pa\,s}]$	$A\,[10^{19}\,\mathrm{Pa\,s}]$	$B\,[10^{-2}\,\mathrm{K^{-1}}]$
1	28.78	6.291
2	20.46	5.912
5	13.04	5.412
10	9.273	5.033
20	6.594	4.654
50	4.202	4.153
100	2.988	3.775

Table 4.2: Exponential dependence parameters for various minimal viscosities.

As an initial condition we use linear temperature distribution from 90 K on the surface to 273 K at the CMB and remaining at that value further below. In the following, we provide an overview of the results obtained through our simulation of thermal evolution of Enceladus with constant orbital eccentricity as well as with the eccentricity evolution equation (2.41) encompassed.

Isotope	^{40}K	^{232}Th	^{235}U	^{238}U
Half-life τ [Ma]	1277	14030	703.81	4468
Initial power per unit mass h_0 [10^{-6} W kg^{-1}]	29.17	26.38	568.7	94.65
Concentration among silicates c [10^{-9}]	1104	53.8	8.2	26.2

Table 4.3: Parameters of LLRI.

4.1 Thermal evolution with constant eccentricity

It is very difficult to balance the entry parameters right so that we get a stable result on long time scale. Mostly, the body of Enceladus will either freeze, or overheat (so-called thermal runaway). In both cases, the used model loses its applicability - the former means the water at the CMB freezes, while the latter emphasizes the role of convection in the body which is not incorporated in our model. Therefore, we terminate the run of the program if the maximum temperature over the body $T_{\max} < 250\,\mathrm{K}$ or $T_{\max} > 500\,\mathrm{K}$ and label them as freeze or runaway, respectively. Thus, instead of searching for a balance, we mapped the space of free parameters $\eta_{\min}$ and e according to the type of evolution scenario.

Results of the computation are most readily summed up in figure 4.1. The blue dots mean freezing of the moon, whereas the red dots are runaway scenarios. It is obvious that Enceladus freezes for higher viscosities and lower eccentricities and overheats vice-versa. Furthermore, for both $e = e_0$ and $\eta_{\min} > 5 \times 10^{14}\,\mathrm{Pa\,s}$ only freezing occurs. Also, there exists an evident continuous border in the parameter space between the two scenarios.

Let us take a closer look at the runaways. In figure 4.2, which shows a comparison of evolution of the maximum temperatures for $\eta_{\min} = 10^{13}\,\mathrm{Pa\,s}$ and different eccentricities, we can see that the temperatures are almost constant, initially, however, this is followed by steep growth, both sooner and more rapid, for higher eccentricities. Figure 4.3 depicts similar curves for $e = 5e_0$ and various minimal viscosities. The growth is almost linear here, and it can be seen that the curves grow much faster for lower viscosities.

Figures 4.4 and 4.5 illustrate a similar comparison to the previous graphs, but now for the average temperatures over the whole body of Enceladus. Here, we can see, except the same steeper trend for higher eccentricities and lower viscosities, that the slower the moon overheats, the higher average temperature it ends up with. For the coldest scenarios, the average temperatures actually decrease to about 202 K for a while at the beginning, only to rise later, ending up at higher values, by the time the terminating condition is satisfied, than their hotter counterparts. For the scenario with $e = 5e_0$ and $\eta_{\min} = 2 \times 10^{14}\,\mathrm{Pa\,s}$, the final temperature reaches almost 230 K.

Finally, figures 4.6 and 4.7 depict an analogous comparison of the thermal production evolution. It is again visible that the generated power grows far faster for higher eccentricities. The coldest scenarios in both figures are actually starting with the heat output greater than the input and, thus, negative thermal production. Generated power in the hottest scenario of $e = 5e_0$ and $\eta_{\min} = 10^{13}\,\mathrm{Pa\,s}$ gets almost as high as 150 GW by the time the maximum temperature

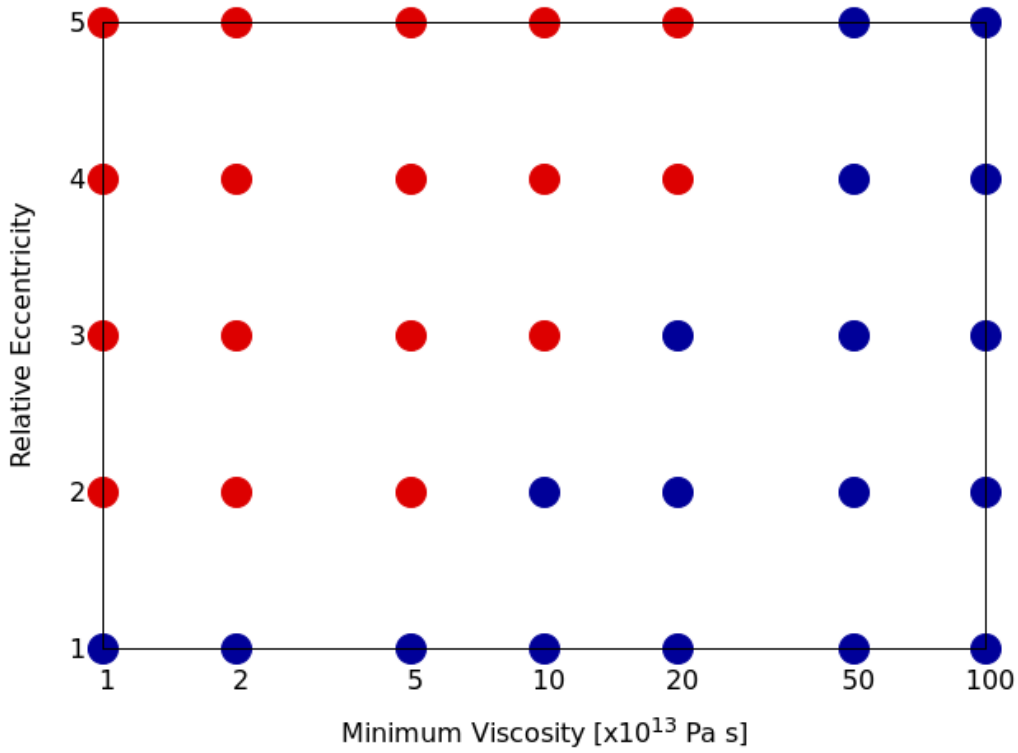

Figure 4.1: Thermal evolution scenario dependence on minimal viscosity and eccentricity. The blue dots mean freezing of the body, while the red ones symbolize thermal runaway. In this chapter, the relative eccentricity is always with regard to the current eccentricity of Enceladus.

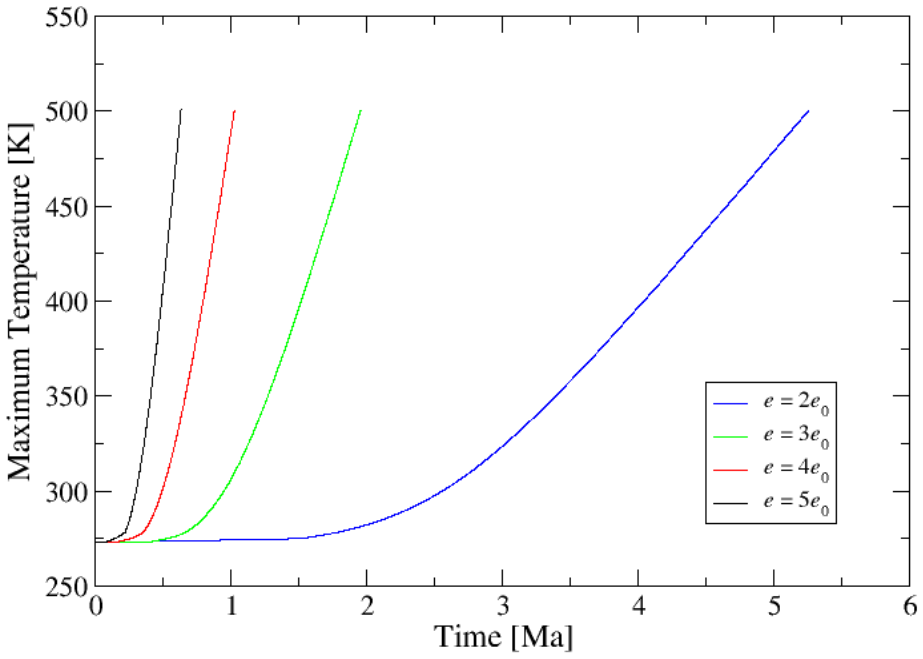

Figure 4.2: Maximum temperature evolution for $\eta_{\min} = 10^{13}\,\mathrm{Pa\,s}$ and various eccentricities.

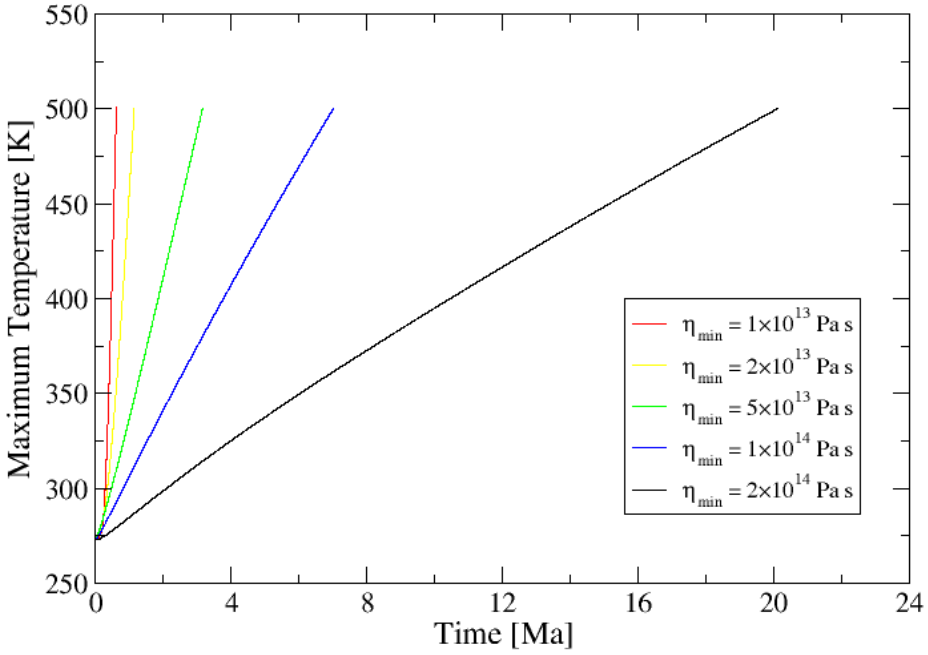

Figure 4.3: Maximum temperature evolution for $e = 5e_0$ and various minimal viscosities.

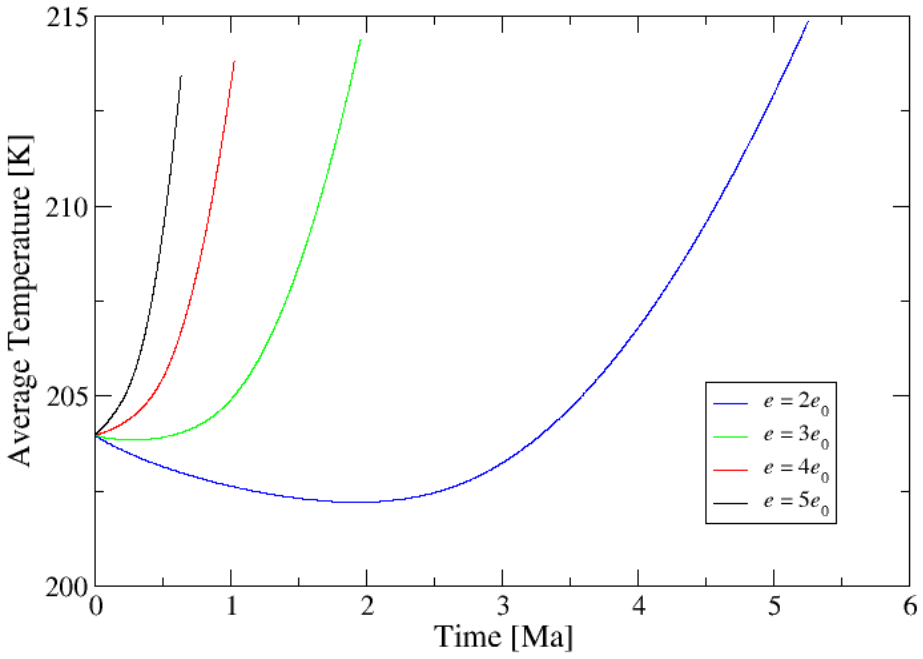

Figure 4.4: Average temperature evolution for $\eta_{\min} = 10^{13}\,\mathrm{Pa\,s}$ and various eccentricities.

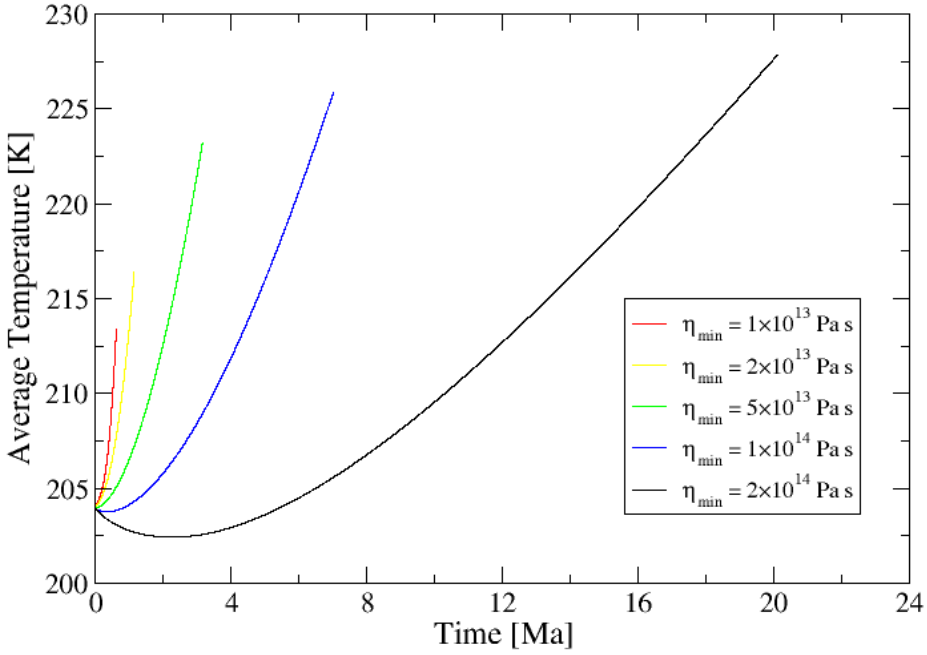

Figure 4.5: Average temperature evolution for $e = 5e_0$ and various minimal viscosities.

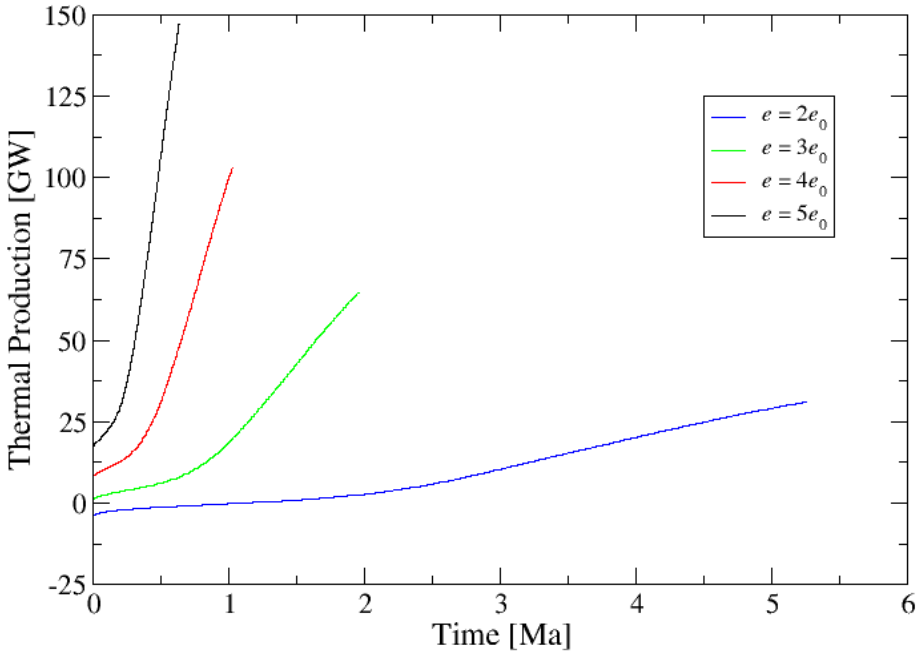

Figure 4.6: Thermal production evolution for $\eta_{\min} = 10^{13}$ Pa s and various eccentricities.

reaches the runaway condition.

On the other hand, all the freezing scenarios behave almost identically, due to prevalence of the LLRI decay over essentially negligible tidal dissipation. That is, why we show only the graphs for $\eta_{\min} = 10^{15}$ Pa s and $e = e_0$ for illustration. In figure 4.8, there can be seen a steady decrease of the average temperature following the more rapid beginning. The maximum temperature, however, grows for about the first 100 million years to almost 350 K, but falls, afterwards, at a quicker rate than the former. Figure 4.9 demonstrates that although the power output in the form of heat flow through the surface gradually declines from its huge initial values almost to the value of the generated input, it remains higher, resulting in negative thermal production. The input also decreases, steadily and slowly, with time.

Now, let us take a slightly different look at the things. In figure 4.10, we compare the times until the runaway is reached for various viscosities and eccentricities. This follows the already mentioned trend of bodies that heat faster having lower viscosity and greater eccentricity. We can also see that time differences are greater between two low eccentricities than between two higher of equal difference, and inversely for viscosities. Regarding to this, it is also visible that sometimes a small eccentricity change can speed up the heating rate by almost four times, e.g. the runaway times for $\eta_{\min} = 5 \times 10^{13}$ Pa s and $e = 2e_0$ and $e = 3e_0$.

Similarly, figure 4.11 shows the times until meeting the freeze condition of the body as defined above. It can be seen that the relative time differences

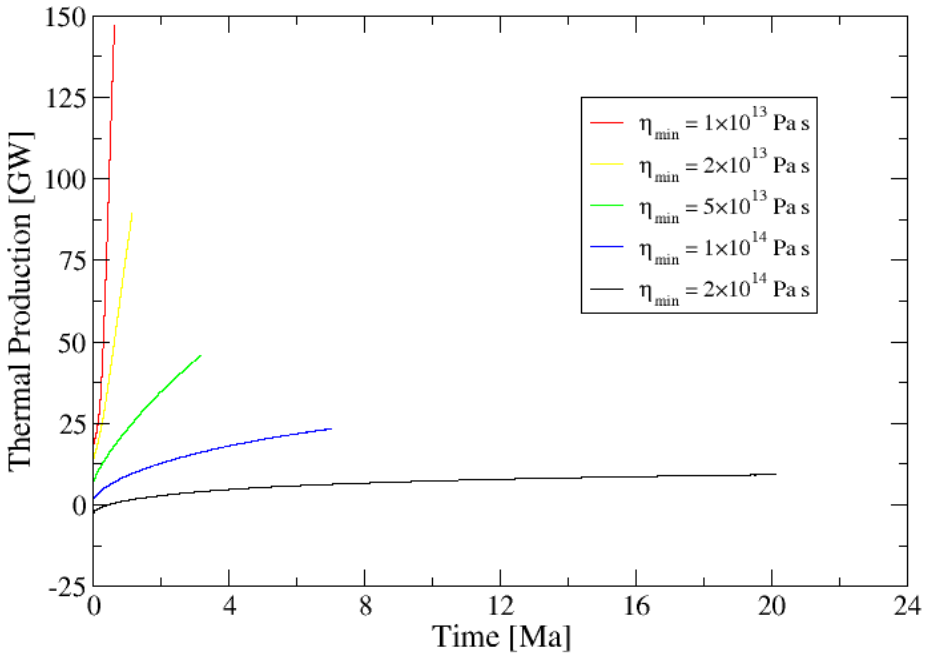

Figure 4.7: Thermal production evolution for $e = 5e_0$ and various minimal viscosities.

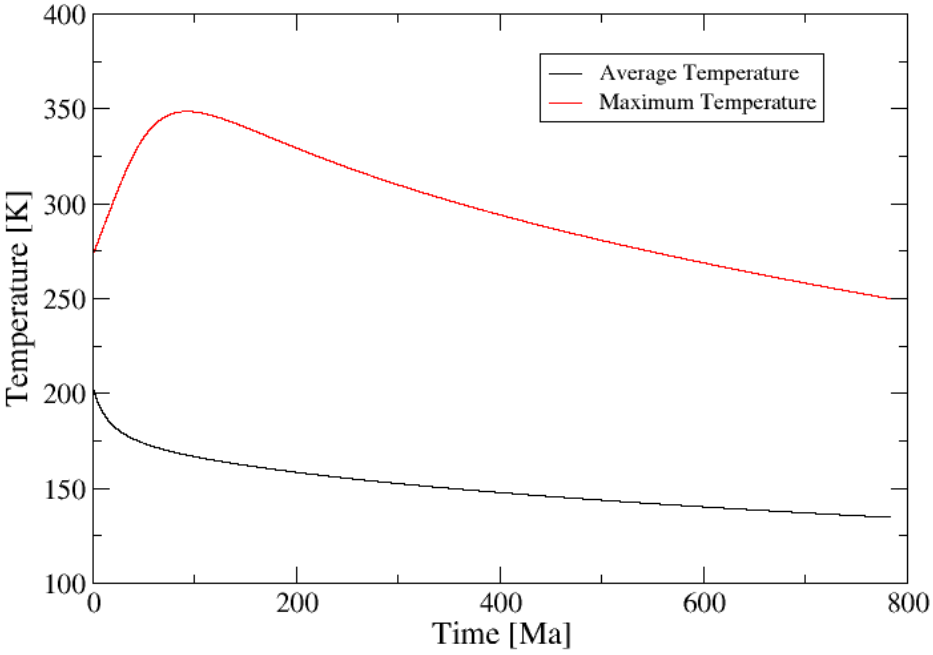

Figure 4.8: Temperature evolution for the freezing scenario with $\eta_{\min} = \times 10^{15}$ Pa s and $e = e_0$.

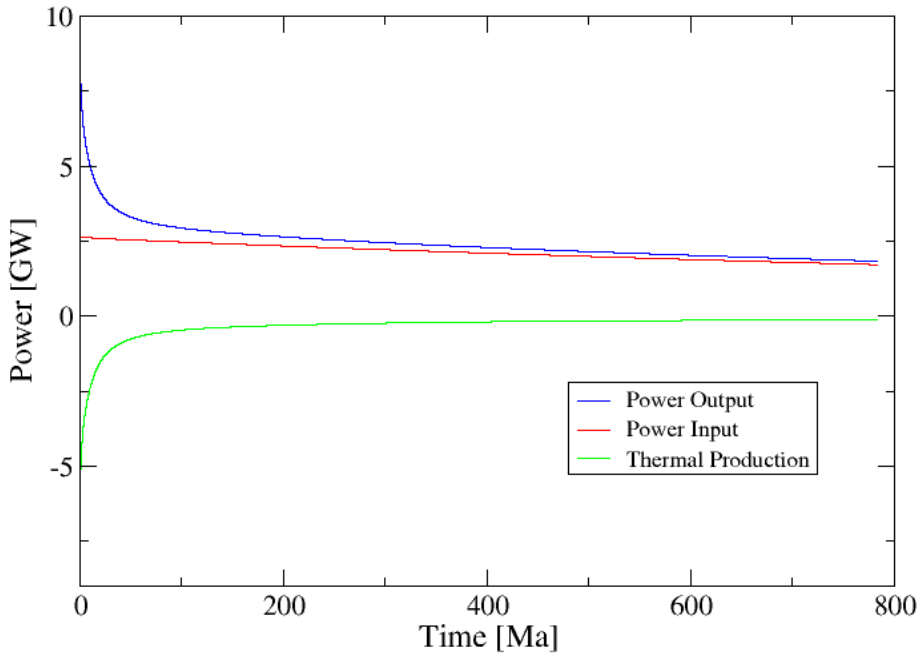

Figure 4.9: Power output, input and thermal production evolution for the freezing scenario with $\eta_{\min} = 10^{15}\,\mathrm{Pa\,s}$ and $e = e_0$.

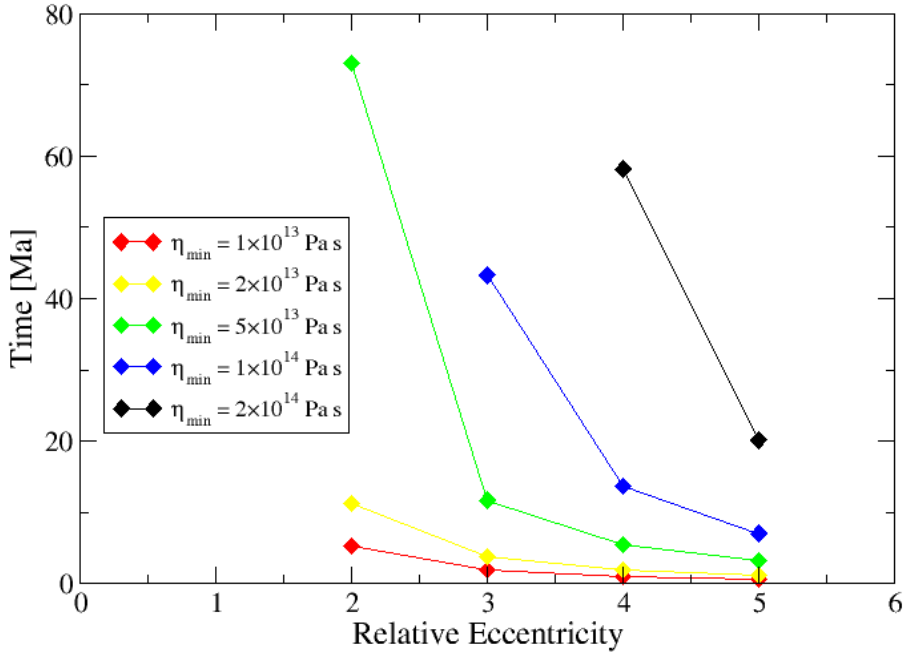

Figure 4.10: Time until reaching thermal runaway for various viscosities and eccentricities.

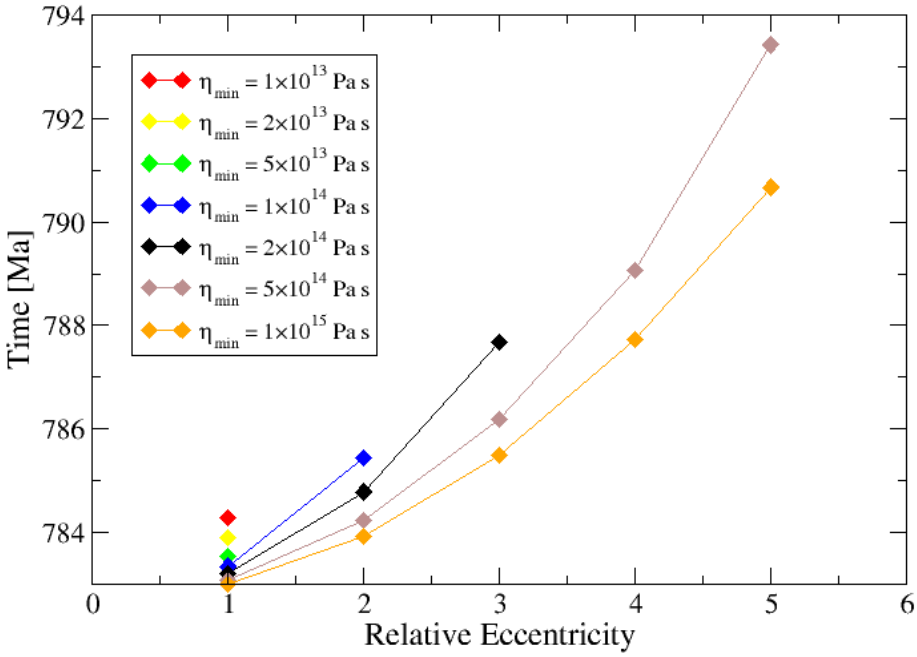

Figure 4.11: Time until reaching the freeze condition for various viscosities and eccentricities.

here are significantly smaller than for the runaways. Cooling is faster for higher viscosities and lower eccentricities and, oppositely to the previous case, time differences between two high eccentricities are bigger than between two lower of equal difference, and again inversely for the viscosities.

4.2 Thermal evolution with changing eccentricity

We further performed computations involving orbital eccentricity evolution. Additional parameters used are noted in table 4.4. In all the computations de-

Radius of Saturn	$R_{\saturn}$	58.232×10^6	km
Mass of Saturn	$M_{\saturn}$	5.6846×10^{26}	kg
Love number of Saturn	$k_2^{\saturn}$	0.32	
Dissipation factor of Saturn	$Q_{\saturn}$	18000	
Radius of Dione	R_{d}	561400	km
Mass of Dione	M_{d}	1.09545×10^{21}	kg
Semi-major axis of Dione	a_{d}	377.396×10^6	km
Semi-major axis of Enceladus	a	237.948×10^6	km

Table 4.4: Parameters used for orbital eccentricity evolution computation.

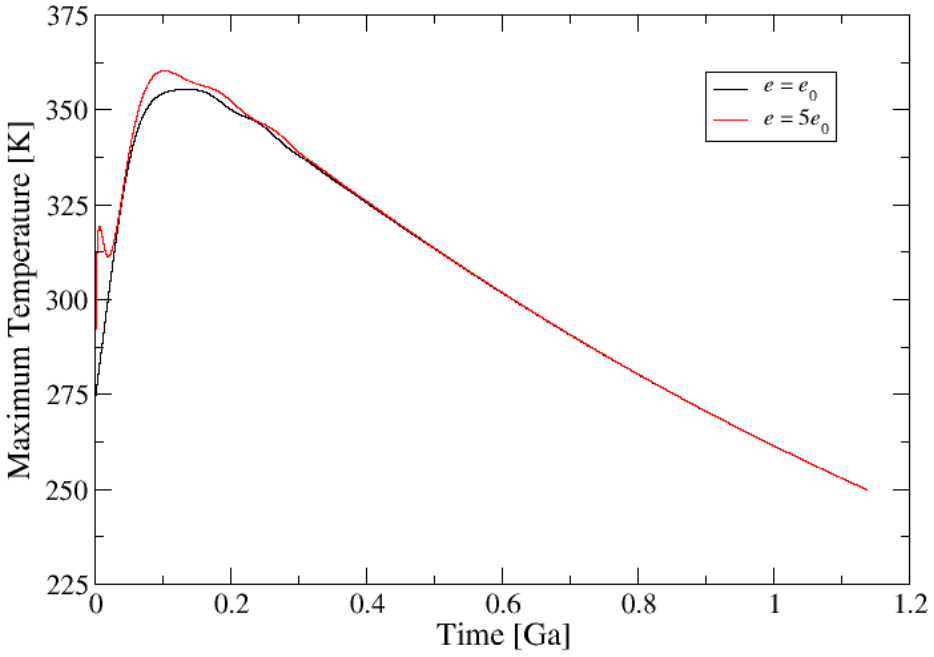

Figure 4.12: Maximum temperature evolution with eccentricity evolution included for two different initial eccentricities.

scribed further, the value of $\eta_{\min} = 10^{13}$ Pa s was used.

Figures 4.12, 4.13, 4.14 and 4.15 compare the evolution of maximum and average temperature, thermal production and eccentricity, respectively, for the initial eccentricity $e_i = e_0$ and $e_i = 5e_0$. On all of them, very similar patterns can be observed. Mainly, oscillations emerge everywhere, due to the feedback between tidal dissipation and eccentricity magnitude. Although the curves seem to be shifted initially, with the one for greater initial eccentricity lagging behind, after about 500 Ga, the oscillations fade out and the same stabilized scenario occurs for both initial conditions: After the oscillation damping, we can see an almost steady growth of eccentricity and decline of temperature while thermal production is slowly growing to zero. Simulation finishes by freezing of Enceladus.

In the last numerical experiment, we added a time-independent, homogeneously distributed heat source in the core of total power H_C. The following figures compare thermal evolution scenarios for Enceladus for different H_C values. As initial eccentricity is used its current value.

Figures 4.16 and 4.17 show maximum and average temperature progression. All the curves on both graphs show very similar behavior, initially boosting up, then peaking and slowly fading afterwards. The most dominant part of the graphs is oscillating behavior occurring the sooner, the lesser is H_C: e.g. basically immediately in $t = 0$ for $H_C = 0$ vs only after 1.5 Ga for the strongest depicted power source $H_C = 1.5$ GW. However, the oscillations always follow the general pattern, for $H_C = 0$ even emerging right during the initial peak. We can see that the maximum temperature reaches the freeze condition for H_C of 1 GW or lesser.

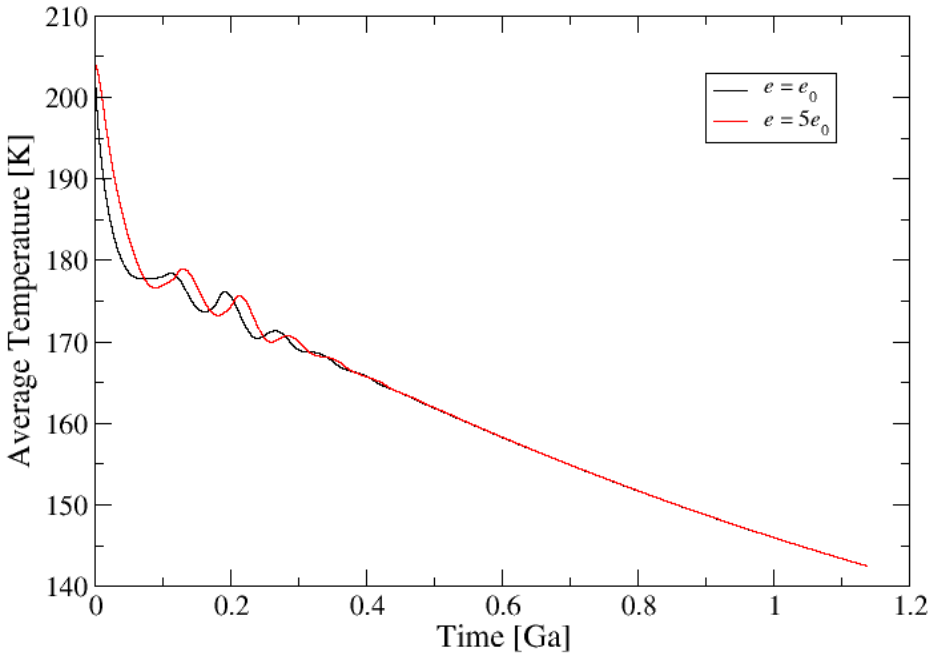

Figure 4.13: Average temperature evolution with eccentricity evolution included for two different initial eccentricities.

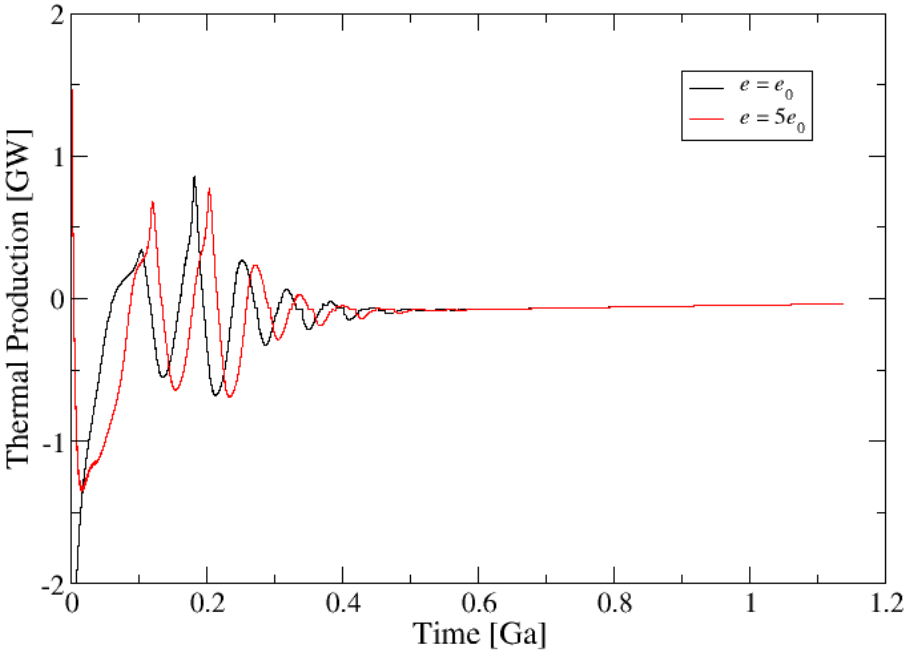

Figure 4.14: Thermal production evolution with eccentricity evolution included for two different initial eccentricities.

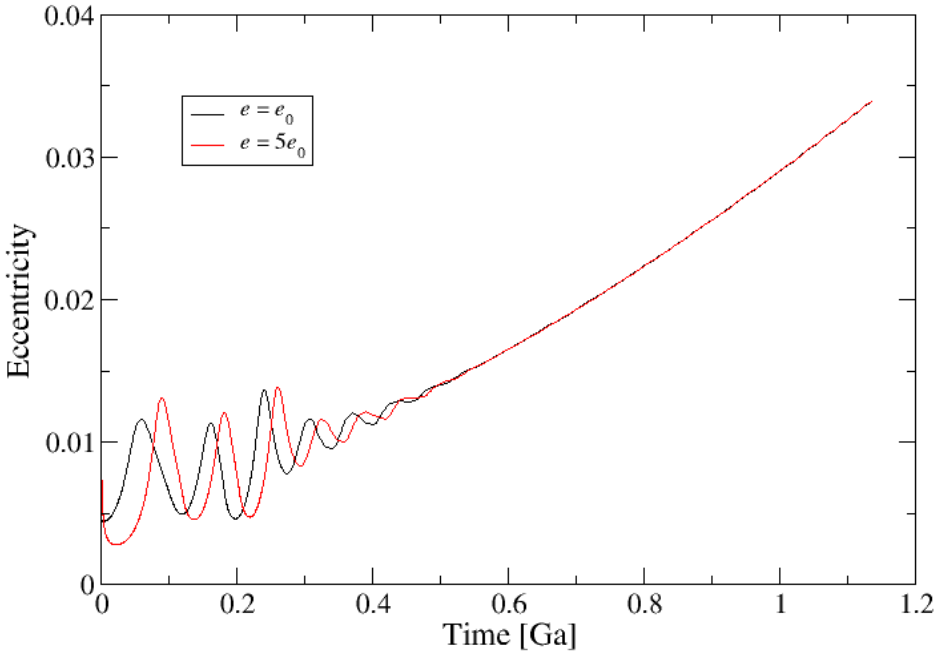

Figure 4.15: Orbital eccentricity evolution for two different initial eccentricities.

For $H_C = 2\,\mathrm{GW}$, we have quick runaway. The most interesting behavior occurs for $H_C = 1.5\,\mathrm{GW}$, where, although the system is getting colder slowly, it still has not frozen after 4 Ga, with the final maximum temperature at that time of above 275 K.

Figure 4.18 describes thermal production evolution. After the initial kick, the systems are slowly stabilizing at roughly the same constant value near zero, however, after some time, the oscillations manifest themselves more strongly than for the temperatures. After their dampening, the system's heat balance values stabilize again, all to a similar value around zero, with occasional small, seemingly chaotic deviations.

Finally, figure 4.19 depicts the eccentricity changes. It is obvious that the higher H_C is, the lower the eccentricity is in any time and the more slowly it grows. Again, we see oscillations corresponding to those on the previous figures and we can observe how they dump after some time, however, rather than perfectly stabilized growth, a somewhat chaotic behavior along the line of continuous growth follows, similar to that for thermal production.

4.3 Discussion

We investigated the parameter space of constant eccentricity e and minimal viscosity η_{min} for the character of the resulting scenarios as well as took a closer look at the properties of some of them. The most important finding here was that, for the current eccentricity value, Enceladus freezes in under 1 Ga, therefore it

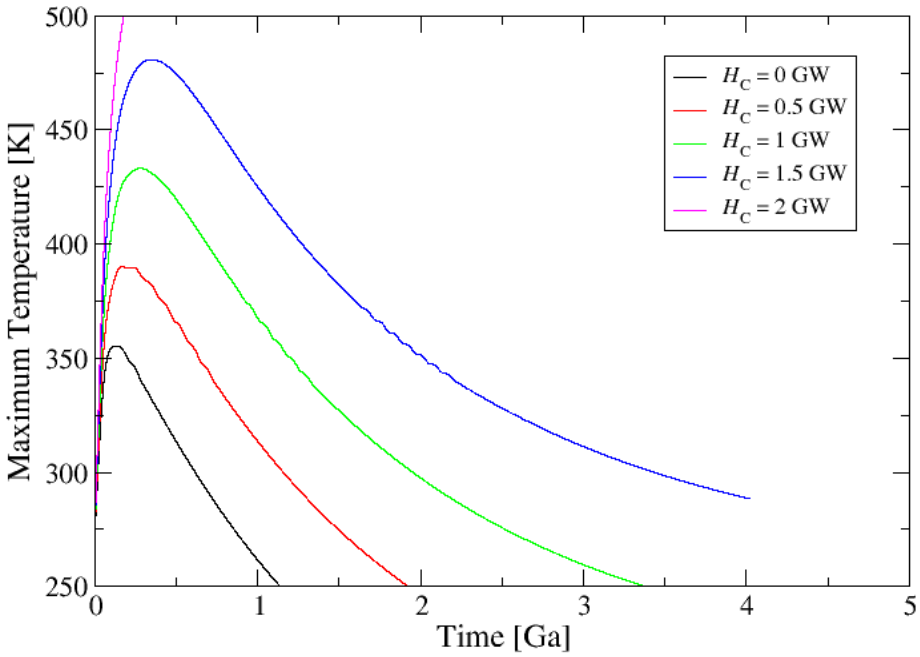

Figure 4.16: Maximum temperature evolution for various core heat source magnitudes.

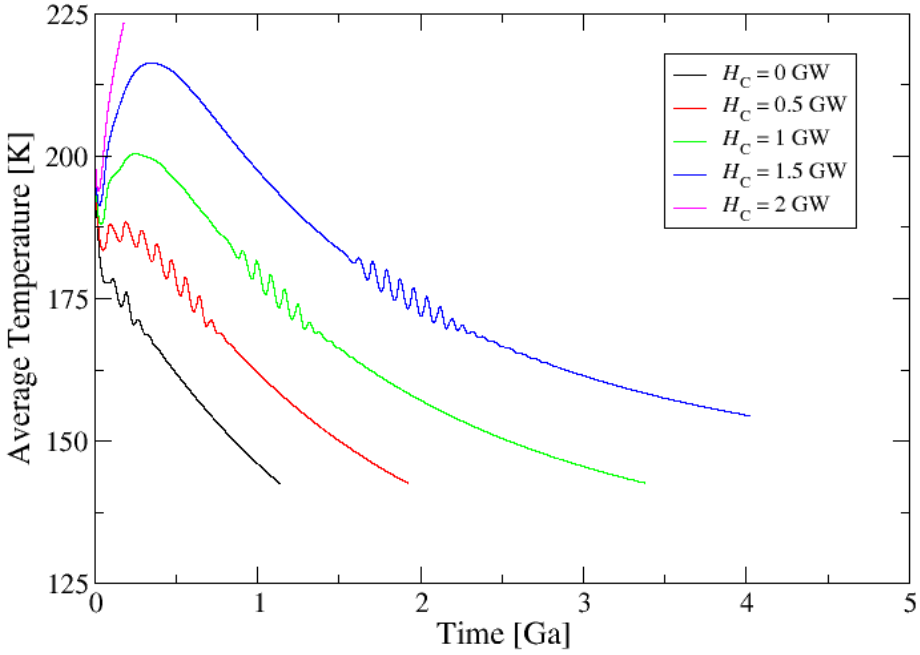

Figure 4.17: Average temperature evolution for various core heat source magnitudes.

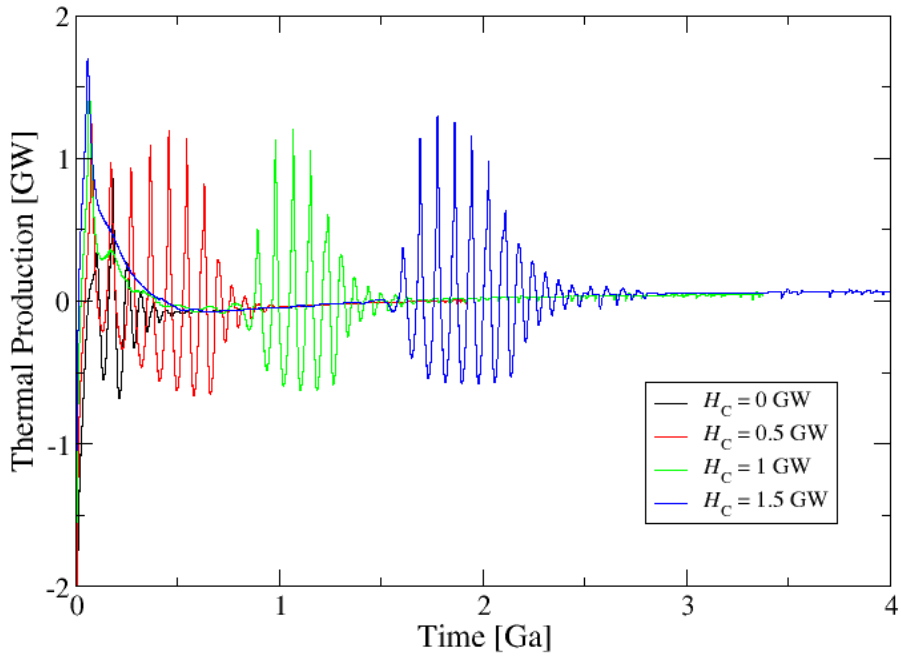

Figure 4.18: Thermal production scenarios for various core heat source magnitudes.

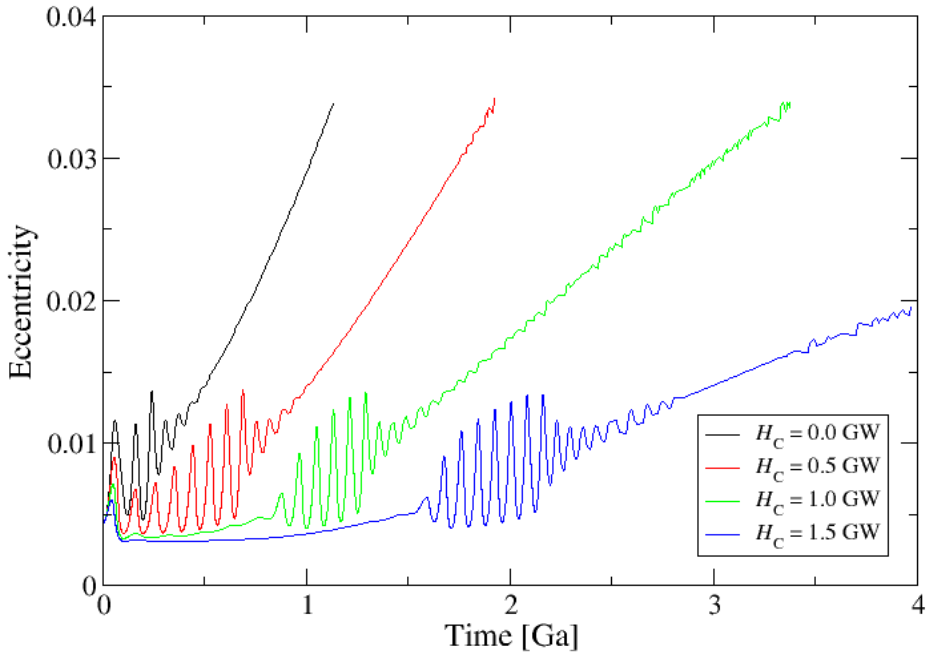

Figure 4.19: Orbital eccentricity evolution for various core heat source magnitudes.

would be unable for it to sustain thermal activity since its formation up to the present time if maintaining the current eccentricity. These scenarios show a steep increase in temperature as the heat from LLRI decay in the core spreads through the mantle, however, soon it begins to escape through the surface, fatally cooling the moon. Our results also show that, however the LLRI isotopes obviously extend the time until freezing, greatly exceeding the tidal dissipation power for the cold scenarios, they still do not provide enough power for the case of $e = e_0$.

Incorporation of the eccentricity evolution equation exposes that, in fact, the initial eccentricity does not matter for the true character of the evolution scenario. Moreover, even for the lowest $\eta_{\min} = 10^{13}\,\mathrm{Pa\,s}$ and both $e_i = e_0$ and $e_i = 5e_0$, Enceladus freezes, quickly. However, after employing the additional heat source in the core as the current research in the field implies (see e.g. [2]), we managed to found a scenario being able to maintain maximum temperature of about 280 K, what would be warm enough for liquid water to be present. Albeit, this was a temperature in the moon's center, while the icy shell being already cold with low dissipation, as the increasing eccentricity suggests.

Now, let us remark the most significant simplifications we used in our model. Firstly, we assumed a global ocean, although the most plausible theories nowadays claim that there is only a local sea present, under the south pole of Enceladus. Secondly, we did not accounted for thermal convection which may exist on Enceladus, particularly because of an enormous extension of the computation process this would imply. On the other hand, the eccentricity evolution equation we used was derived using the assumption of convection prevalence over the conductive heat transport (see [12]). The assumption of angularly-independent physical parameters is also not absolutely right, taking into consideration just that many of the parameters we used are functions of temperature which was non-homogeneously distributed over the layers. Finally, speaking about the temperature, there is still possibility of more precise computation, figuring in the spherical decomposition components of dissipation sources of $j > 2$.

Conclusion

Our work is to be summarized in the following points:

- We used a mathematical model of a continuous body characterized by Maxwell viscoelasticity and heat conduction and incorporated it into a Fortran program for computation of tidal dissipation and heat transport in Saturn's moon Enceladus, with an option to encompass orbital eccentricity evolution. We did it using the spectral method, in 3D, with restrictions on some parameters to be only radially-dependent. We also included the effect of long-lived radioactive isotopes decay in the core on the total heat produced.

- We calculated thermal evolution of the satellite for different initial eccentricity and minimal viscosity values. We divided the space of the two parameters into two regions: where the body of Enceladus overheats and where it freezes. We further examined the characteristics of chosen scenarios.

- We showed that if the eccentricity evolution is involved, the initial eccentricity has no effect on the final result and Enceladus will always freeze.

- We discovered that if another homogeneous heat source in the core is added, a scenario can be found, in which the moon does not freeze in 4 Ga, what is the time scale needed to maintain thermal activity in the present.

Future research in the area could include further examination of the transition region we found between the hot and cold scenarios for constant orbital eccentricity as well as of the suitable power magnitudes of the homogeneous heat source in the core for the variable value. Moreover, including the coefficients of degree $j > 2$ of spectral decomposition of dissipated power could increase the calculation precision. Probably the most difficult but also the most valuable addition would be incorporating a full 3D model with angularly dependent viscosity and other, now restricted, parameters and only locally present subsurface water ocean.

A. Appendix

Here, we provide a brief summary of the mathematics regarding scalar, vector and tensor harmonics as well as some useful identities we use in our computations. The source for the sub-chapters A.1 and A.3 is, except when cited otherwise, [7]. For sub-chapter A.2, the source is [13].

A.1 Spherical harmonics

Let S be a unit sphere (parametrized by polar and azimuthal angles ϑ and φ) defined in the three-dimensional Euclidean space E_3 and let $\boldsymbol{X}^\infty$ be a space of smooth complex functions on S. We define the *scalar spherical harmonics* as

$$Y_{jm}(\vartheta,\varphi) = (-1)^m N_{jm} P_{jm}(\cos\vartheta)\, e^{im\varphi};\ \text{for}\ j = 0,1,\ldots,\infty;\ m = 0,\ldots,j \quad \text{(A.1)}$$

and

$$Y_{jm}(\vartheta,\varphi) = (-1)^m Y^*_{j|m|}(\vartheta,\varphi); \quad \text{for}\, m = -j,\ldots,0, \quad \text{(A.2)}$$

where $P_{jm}(\cos\vartheta)$ are the associated Legendre polynomials and

$$N_{jm} = \left[\frac{(2j+1)}{4\pi}\frac{(j-m)!}{(j+m)!}\right]^{1/2} \quad \text{(A.3)}$$

are normalization factors such that the orthonormality condition

$$\int_0^\pi \int_0^{2\pi} Y_{j_1m_1}(\vartheta,\varphi) Y^*_{j_2m_2}(\vartheta,\varphi)\sin\vartheta\,\mathrm{d}\varphi\,\mathrm{d}\vartheta = \delta_{j_1j_2}\delta_{m_1m_2} \quad \text{(A.4)}$$

is satisfied. Every complex function $f(r,\vartheta,\varphi) \in L^2(E_1 \times S)$ can be expanded into a series

$$f(r,\vartheta,\varphi) = \sum_{j=0}^{\infty}\sum_{m=-j}^{j} f_{jm}(r) Y_{jm}(\vartheta,\varphi), \quad \text{(A.5)}$$

also called the spectral series, where

$$f_{jm}(r) = \int_0^\pi \int_0^{2\pi} f(r,\vartheta,\varphi) Y^*_{jm}(\vartheta,\varphi)\sin\vartheta\,\mathrm{d}\varphi\,\mathrm{d}\vartheta \quad \text{(A.6)}$$

are the scalar spherical coefficients. Furthermore, for $f(r,\vartheta,\varphi)$ being a real function, the following symmetry holds:

$$f_{j-m} = (-1)^m f^*_{jm}. \quad \text{(A.7)}$$

Let us now define a basis of E_3 in the form

$$\begin{aligned} \vec{e}_1 &= \frac{-1}{\sqrt{2}}\left(\vec{e}_x + i\vec{e}_y\right), \\ \vec{e}_0 &= \vec{e}_z, \\ \vec{e}_{-1} &= \frac{1}{\sqrt{2}}\left(\vec{e}_x - i\vec{e}_y\right), \end{aligned} \quad \text{(A.8)}$$

where $\vec{e}_x$, $\vec{e}_y$, $\vec{e}_z$ are Cartesian unit vectors. We define the *vector spherical harmonics* as

$$\boldsymbol{Y}^l_{jm}(\vartheta,\varphi) = \sum_{\mu=-1}^{1}\sum_{\nu=-l}^{l} C^{jm}_{l\nu 1\mu} Y_{l\nu}\left(\vartheta,\varphi\right)\vec{e}_\mu, \tag{A.9}$$

where $j = 0, 1, \ldots, \infty$; $m = -j, \ldots, j$; $l = |j-1|, j, j+1$ and $C^{jm}_{l\nu 1\mu}$ are the Clebsch-Gordan coefficients. Also, a symmetry in the form of

$$\boldsymbol{Y}^l_{j-m} = (-1)^{j+m+l+1}\boldsymbol{Y}^{l\,*}_{jm} \tag{A.10}$$

is satisfied. Similarly to the scalar harmonics, the orthonormality condition

$$\int_0^\pi\int_0^{2\pi} \boldsymbol{Y}^{l_1}_{j_1m_1}(\vartheta,\varphi)\cdot\boldsymbol{Y}^{l_2*}_{j_2m_2}(\vartheta,\varphi)\sin\vartheta\,\mathrm{d}\varphi\,\mathrm{d}\vartheta = \delta_{j_1j_2}\delta_{m_1m_2}\delta_{l_1l_2} \tag{A.11}$$

holds. Also, every complex vector function $\vec{f}(r,\vartheta,\varphi) \in L^2(E_1\times S)$ can be decomposed into a series

$$\vec{f}(r,\vartheta,\varphi) = \sum_{j=0}^{\infty}\sum_{m=-j}^{j}\sum_{l=|j-1|}^{j+1} f^l_{jm}(r)\boldsymbol{Y}^l_{jm}(\vartheta,\varphi), \tag{A.12}$$

with $f^l_{jm}(r)$ being the vector spherical coefficients. If, moreover, the function is real, then

$$f^l_{j-m} = (-1)^{j+m+l+1}f^{l\,*}_{jm} \tag{A.13}$$

is true.

Finally, we define

$$\boldsymbol{e}_{k\lambda} = \sum_{\mu=-1}^{1}\sum_{\nu=-1}^{1} C^{k\lambda}_{1\mu 1\nu}\vec{e}_\mu\vec{e}_\nu, \tag{A.14}$$

where $k = 0, 1, 2$ and $\lambda = -k, \ldots, k$, and the *tensor spherical harmonics* as

$$\boldsymbol{Y}^{lk}_{jm}(\vartheta,\varphi) = \sum_{\mu=-l}^{l}\sum_{\nu=-k}^{k} C^{jm}_{l\mu k\nu} Y_{l\mu}\left(\vartheta,\varphi\right)\boldsymbol{e}_{k\nu}, \tag{A.15}$$

where $j = 0, 1, \ldots, \infty$; $m = -j, \ldots, j$; $k = 0, 1, 2$ and $l = |j-k|, j, j+k$. The orthonormality condition of

$$\int_0^\pi\int_0^{2\pi} \boldsymbol{Y}^{l_1k_1}_{j_1m_1}(\vartheta,\varphi) : \boldsymbol{Y}^{l_2k_2*}_{j_2m_2}(\vartheta,\varphi)\sin\vartheta\,\mathrm{d}\varphi\,\mathrm{d}\vartheta = \delta_{j_1j_2}\delta_{m_1m_2}\delta_{l_1l_2} \tag{A.16}$$

holds. Any complex tensor function $\boldsymbol{f}(r,\vartheta,\varphi) \in L^2(E_1\times S)$ can be written in the form

$$\boldsymbol{f}(r,\vartheta,\varphi) = \sum_{j=0}^{\infty}\sum_{m=-j}^{j}\sum_{k=0}^{2}\sum_{l=|j-k|}^{j+k} f^{lk}_{jm}(r)\boldsymbol{Y}^{lk}_{jm}(\vartheta,\varphi), \tag{A.17}$$

with the tensor spherical coefficients $f^{lk}_{jm}(r)$.

A.2 Clebsch-Gordan coefficients and Wigner symbols

The 6-j Wigner symbol is defined as

$$\begin{Bmatrix} j_1 & j_2 & j \\ l_1 & l_2 & l \end{Bmatrix} = \frac{(-1)^{j_1+j_2+l_1+l_2}}{\Pi_{jl}} \times \\ \times \sum_{m_1,m_2,m} \sum_{k_1,k_2,k} C^{l_2 k_2}_{jml_1k_1} C^{jm}_{j_1 m_1 j_2 m_2} C^{l_2 k_2}_{j_1 m_1 lk} C^{lk}_{j_2 m_2 l_1 k_1}, \quad \text{(A.18)}$$

where

$$\Pi_{j_1,j_2,\ldots,j_n} = \prod_{i=1}^{n} \sqrt{2j_i+1}. \quad \text{(A.19)}$$

The 6-j symbol is invariant under the permutation of any two columns or the upper and lower arguments in any two columns.

We define the 9-j Wigner symbol as

$$\begin{Bmatrix} j_{11} & j_{12} & j_{13} \\ j_{21} & j_{22} & j_{23} \\ j_{31} & j_{32} & j_{33} \end{Bmatrix} = \sum_{r\in\mathbb{Z}} (-1)^r (2r+1) \times \\ \times \begin{Bmatrix} j_{11} & j_{21} & j_{31} \\ j_{32} & j_{33} & r \end{Bmatrix} \begin{Bmatrix} j_{12} & j_{22} & j_{32} \\ j_{21} & r & j_{23} \end{Bmatrix} \begin{Bmatrix} j_{13} & j_{23} & j_{33} \\ r & j_{11} & j_{12} \end{Bmatrix}. \quad \text{(A.20)}$$

It is invariant under the reflection in each diagonal or two consecutive permutations of any two rows or any two columns.

The objects above also satisfy the following relations:

$$C^{jm}_{j_1 m_1 j_2 m_2} \neq 0 \quad \Rightarrow \quad j = |j_1 - j_2|, \ldots, j_1 + j_2, \quad \text{(A.21)}$$

$$C^{jm}_{j_1 m_1 00} = \delta_{jj_1}\delta_{mm_1}, \quad \text{(A.22)}$$

$$C^{jm}_{j_1 m_1 j_2 m_2} = (-1)^{j+j_1+j_2} C^{jm}_{j_2 m_2 j_1 m_1}, \quad \text{(A.23)}$$

$$\begin{Bmatrix} j_1 & j_2 & j \\ l_1 & l_2 & 0 \end{Bmatrix} = \frac{(-1)^{j_1+j_2+j}}{\Pi_{j_1 j_2}} \delta_{j_1 l_2} \delta_{j_2 l_1}, \quad \text{(A.24)}$$

$$\begin{Bmatrix} 0 & j & j \\ l & k_1 & k_2 \\ l & k_3 & k_4 \end{Bmatrix} = \frac{(-1)^{j+l+k_2+k_3}}{\Pi_{jl}} \begin{Bmatrix} k_4 & k_2 & j \\ k_1 & k_3 & l \end{Bmatrix}. \quad \text{(A.25)}$$

A.3 Useful formulas with spherical harmonics

Here, we bring a short list of spherical harmonics identities used in the thesis.

$$\vec{e}_r Y_{jm} = \frac{1}{\sqrt{2j+1}} \left(\sqrt{j}\, \delta_{l,j-1} - \sqrt{j+1}\, \delta_{l,j+1} \right) \boldsymbol{Y}^l_{jm} \quad \text{(A.26)}$$

$$\vec{e}_r \cdot \boldsymbol{Y}^l_{jm} = \frac{1}{\sqrt{2j+1}} \left(\sqrt{j}\, \delta_{l,j-1} - \sqrt{j+1}\, \delta_{l,j+1} \right) Y_{jm} \quad \text{(A.27)}$$

$$\vec{e}_r \cdot \boldsymbol{Y}_{jm}^{j0} = \frac{1}{\sqrt{3(2j+1)}} \left(\sqrt{j+1}\, \boldsymbol{Y}_{jm}^{j+1} - \sqrt{j}\, \boldsymbol{Y}_{jm}^{j-1} \right) \tag{A.28}$$

$$\vec{e}_r \cdot \boldsymbol{Y}_{jm}^{j-2,2} = \sqrt{\frac{j-1}{2j-1}}\, \boldsymbol{Y}_{jm}^{j-1} \tag{A.29}$$

$$\vec{e}_r \cdot \boldsymbol{Y}_{jm}^{j2} = \sqrt{\frac{j(2j-1)}{6(2j+1)(2j+3)}}\, \boldsymbol{Y}_{jm}^{j+1} - \sqrt{\frac{(j+1)(2j+3)}{6(2j+1)(2j-1)}}\, \boldsymbol{Y}_{jm}^{j-1} \tag{A.30}$$

$$\vec{e}_r \cdot \boldsymbol{Y}_{jm}^{j+2,2} = -\sqrt{\frac{j+2}{2j+3}}\, \boldsymbol{Y}_{jm}^{j+1} \tag{A.31}$$

$$\nabla f(r) Y_{jm} = \frac{1}{\sqrt{2j+1}} \Bigg[\sqrt{j} \left(\frac{\mathrm{d}}{\mathrm{d}r} + \frac{j+1}{r} \right) f(r) \boldsymbol{Y}_{jm}^{j-1} - \\ - \sqrt{j+1} \left(\frac{\mathrm{d}}{\mathrm{d}r} - \frac{j}{r} \right) f(r) \boldsymbol{Y}_{jm}^{j+1} \Bigg] \tag{A.32}$$

$$\nabla \cdot f(r) \boldsymbol{Y}_{jm}^{l} = \frac{1}{\sqrt{2j+1}} \Bigg[\sqrt{j} \left(\frac{\mathrm{d}}{\mathrm{d}r} - \frac{j-1}{r} \right) \delta_{l,j-1} - \\ - \sqrt{j+1} \left(\frac{\mathrm{d}}{\mathrm{d}r} + \frac{j+2}{r} \right) \delta_{l,j+1} \Bigg] f(r) Y_{jm} \tag{A.33}$$

$$\nabla \cdot f(r) \boldsymbol{Y}_{jm}^{j0} = -\sqrt{\frac{j}{3(2j+1)}} \left(\frac{\mathrm{d}}{\mathrm{d}r} + \frac{j+1}{r} \right) f(r) \boldsymbol{Y}_{jm}^{j-1} + \\ + \sqrt{\frac{j+1}{3(2j+1)}} \left(\frac{\mathrm{d}}{\mathrm{d}r} - \frac{j}{r} \right) f(r) \boldsymbol{Y}_{jm}^{j+1} \tag{A.34}$$

$$\nabla \cdot f(r) \boldsymbol{Y}_{jm}^{j-2,2} = \sqrt{\frac{j-1}{2j-1}} \left(\frac{\mathrm{d}}{\mathrm{d}r} - \frac{j-2}{r} \right) f(r) \boldsymbol{Y}_{jm}^{j-1} \tag{A.35}$$

$$\nabla \cdot f(r) \boldsymbol{Y}_{jm}^{j2} = -\sqrt{\frac{(j+1)(2j+3)}{6(2j-1)(2j+1)}} \left(\frac{\mathrm{d}}{\mathrm{d}r} + \frac{j+1}{r} \right) f(r) \boldsymbol{Y}_{jm}^{j-1} + \\ + \sqrt{\frac{j(2j-1)}{6(2j+1)(2j+3)}} \left(\frac{\mathrm{d}}{\mathrm{d}r} - \frac{j}{r} \right) f(r) \boldsymbol{Y}_{jm}^{j+1} \tag{A.36}$$

$$\nabla \cdot f(r) \boldsymbol{Y}_{jm}^{j+2,2} = -\sqrt{\frac{j+2}{2j+3}} \left(\frac{\mathrm{d}}{\mathrm{d}r} + \frac{j+3}{r} \right) f(r) \boldsymbol{Y}_{jm}^{j+1} \tag{A.37}$$

$$\boldsymbol{Y}_{j_1 m_1}^{l_1} \cdot \boldsymbol{Y}_{j_2 m_2}^{l_2} = (-1)^{j_2+l_2} \frac{\Pi_{j_1 j_2 l_1 l_2}}{\sqrt{4\pi}} \sum_{jm} \frac{1}{\Pi_j} C_{l_1 0 l_2 0}^{j0} C_{j_1 m_1 j_2 m_2}^{jm} \begin{Bmatrix} j_1 & j_2 & j \\ l_2 & l_1 & 1 \end{Bmatrix} Y_{jm} \tag{A.38}$$

$$\boldsymbol{Y}^{l_1k_1}_{j_1m_1}\cdot\boldsymbol{Y}^{l_2}_{j_2m_2}=(-1)^{k_1+1}\frac{\Pi_{j_1j_2l_1l_2k_1}}{\sqrt{4\pi}}\sum_{jml}C^{l0}_{l_10l_20}C^{jm}_{j_1m_1j_2m_2}\begin{Bmatrix}j & j_1 & j_2\\ l & l_1 & l_2\\ 1 & k_1 & 1\end{Bmatrix}\boldsymbol{Y}^{l}_{jm} \quad \text{(A.39)}$$

Moreover, the symmetric traceless part of the gradient of a vector can be expressed as [14]

$$\begin{aligned}\left[\nabla f(r)\boldsymbol{Y}^{l}_{jm}\right]^{k=2}=&\sqrt{\frac{j-1}{2j-1}}\left(\frac{\mathrm{d}}{\mathrm{d}r}+\frac{j}{r}\right)f(r)\boldsymbol{Y}^{j-2,2}_{jm}\delta_{l,j-1}-\\&-\sqrt{\frac{(j+1)(2j+3)}{6(2j-1)(2j+1)}}\left(\frac{\mathrm{d}}{\mathrm{d}r}-\frac{j-1}{r}\right)f(r)\boldsymbol{Y}^{j,2}_{jm}\delta_{l,j-1}+\\&+\sqrt{\frac{j-1}{2(2j+1)}}\left(\frac{\mathrm{d}}{\mathrm{d}r}+\frac{j+1}{r}\right)f(r)\boldsymbol{Y}^{j-1,2}_{jm}\delta_{l,j}-\\&-\sqrt{\frac{(j+2)}{2(2j+1)}}\left(\frac{\mathrm{d}}{\mathrm{d}r}-\frac{j}{r}\right)f(r)\boldsymbol{Y}^{j+1,2}_{jm}\delta_{l,j}+\\&+\sqrt{\frac{j(2j-1)}{6(2j+1)(2j+3)}}\left(\frac{\mathrm{d}}{\mathrm{d}r}+\frac{j+2}{r}\right)f(r)\boldsymbol{Y}^{j,2}_{jm}\delta_{l,j+1}-\\&-\sqrt{\frac{j+2}{2j+3}}\left(\frac{\mathrm{d}}{\mathrm{d}r}-\frac{j+1}{r}\right)f(r)\boldsymbol{Y}^{j+2,2}_{jm}\delta_{l,j+1}. \quad \text{(A.40)}\end{aligned}$$

A.4 Spectral analysis

Let us have a real tensor function $\boldsymbol{T}$ on a sphere, written in the form of spectral series

$$\boldsymbol{T}=\sum_{j=0}^{\infty}\sum_{m=0}^{j}\sum_{k=0}^{2}\sum_{l=|j-k|}^{j+k}T^{lk}_{jm}\boldsymbol{Y}^{lk}_{jm}. \quad \text{(A.41)}$$

Here, we provide the relations for expressing of its Cartesian coordinates in the form of scalar spherical harmonic series, also called the spectral analysis.

Firstly, let us express the unit Cartesian vectors from the vector harmonics. Using the Clebsch-Gordan coefficient identities (A.22) and (A.23), we get from the vector harmonics definition (A.9) that

$$\begin{aligned}\boldsymbol{Y}^{0}_{11}&=Y_{00}\vec{e}_1,\\ \boldsymbol{Y}^{0}_{10}&=Y_{00}\vec{e}_0,\\ \boldsymbol{Y}^{0}_{1-1}&=Y_{00}\vec{e}_{-1}\end{aligned} \quad \text{(A.42)}$$

and subsequently, utilizing the definition of the special E_3 basis given by (A.8):

$$\begin{aligned}\vec{e}_x&=\sqrt{2\pi}\left(-\boldsymbol{Y}^{0}_{11}+\boldsymbol{Y}^{0}_{1-1}\right),\\ \vec{e}_y&=i\sqrt{2\pi}\left(\boldsymbol{Y}^{0}_{11}+\boldsymbol{Y}^{0}_{1-1}\right),\\ \vec{e}_z&=2\sqrt{\pi}\boldsymbol{Y}^{0}_{10}.\end{aligned} \quad \text{(A.43)}$$

We compute the Cartesian components T_{ab} of the tensor $\boldsymbol{T}$ as

$$T_{ab}=\vec{e}_a\cdot\boldsymbol{T}\cdot\vec{e}_b=(\boldsymbol{T}\cdot\vec{e}_b)\cdot\vec{e}_a=\vec{T}_b\cdot\vec{e}_a, \quad \text{(A.44)}$$

for any $a, b = x, y, z$. Utilizing the Cartesian basis vectors expression above, identities (A.22), (A.24), (A.25), (A.38), (A.39), triangular rule for Clebsch-Gordan coefficients and 6-j and 9-j Wigner symbols permutation symmetries, we get

$$\begin{aligned}
\vec{T}_x =& \sum_{j_1=0}^{\infty}\sum_{m_1=0}^{j}\sum_{l_1=|j_1-1|}^{j_1+1}(T_x)^{l_1}_{j_1m_1}\boldsymbol{Y}^{l_1}_{j_1m_1} \\
=& \sum_{j_1=0}^{\infty}\sum_{m_1=0}^{j}\sum_{j_0=|j_1-1|}^{j_1+1}\sum_{m_0=0}^{j_0}\sum_{k_0=0}^{2}\sum_{l_1=\max\{|j_0-k|,|j-1|\}}^{\min\{j_0+k,j+1\}}(-1)^{j_1+l_1}\frac{\Pi_{j_0k_0}}{\sqrt{2}}\times \\
&\times\begin{Bmatrix} j_0 & j_1 & 1 \\ 1 & k_0 & l_1 \end{Bmatrix}\Bigg[\left(C^{j_1,m_1}_{j_0,m_0,1,-1}-C^{j_1,m_1}_{j_0,m_0,1,1}\right)T^{l_1k_0}_{j_0m_0}+ \\
&+(\delta_{m_1,0}-1)^{j_1+m_1+l_1+1}\left(C^{j_1,-m_1}_{j_0,m_0,1,-1}-C^{j_1,-m_1}_{j_0,m_0,1,1}\right)\left(T^{l_1k_0}_{j_0m_0}\right)^*\Bigg]\boldsymbol{Y}^{l_1}_{j_1m_1}, \qquad \text{(A.45)}
\end{aligned}$$

$$\begin{aligned}
\vec{T}_y =& \sum_{j_1=0}^{\infty}\sum_{m_1=0}^{j}\sum_{l_1=|j_1-1|}^{j_1+1}(T_y)^{l_1}_{j_1m_1}\boldsymbol{Y}^{l_1}_{j_1m_1} \\
=& \sum_{j_1=0}^{\infty}\sum_{m_1=0}^{j}\sum_{j_0=|j_1-1|}^{j_1+1}\sum_{m_0=0}^{j_0}\sum_{k_0=0}^{2}\sum_{l_1=\max\{|j_0-k|,|j-1|\}}^{\min\{j_0+k,j+1\}}(-1)^{j_1+l_1}\frac{\Pi_{j_0k_0}}{\sqrt{2}}\times \\
&\times\begin{Bmatrix} j_0 & j_1 & 1 \\ 1 & k_0 & l_1 \end{Bmatrix} i\Bigg[\left(C^{j_1,m_1}_{j_0,m_0,1,-1}+C^{j_1,m_1}_{j_0,m_0,1,1}\right)T^{l_1k_0}_{j_0m_0}- \\
&-(\delta_{m_1,0}-1)^{j_1+m_1+l_1+1}\left(C^{j_1,-m_1}_{j_0,m_0,1,-1}+C^{j_1,-m_1}_{j_0,m_0,1,1}\right)\left(T^{l_1k_0}_{j_0m_0}\right)^*\Bigg]\boldsymbol{Y}^{l_1}_{j_1m_1}, \qquad \text{(A.46)}
\end{aligned}$$

$$\begin{aligned}
\vec{T}_z =& \sum_{j_1=0}^{\infty}\sum_{m_1=0}^{j}\sum_{l_1=|j_1-1|}^{j_1+1}(T_z)^{l_1}_{j_1m_1}\boldsymbol{Y}^{l_1}_{j_1m_1} \\
=& \sum_{j_1=0}^{\infty}\sum_{m_1=0}^{j}\sum_{j_0=|j_1-1|}^{j_1+1}\sum_{m_0=0}^{j_0}\sum_{k_0=0}^{2}\sum_{l_1=\max\{|j_0-k|,|j-1|\}}^{\min\{j_0+k,j+1\}}(-1)^{j_1+l_1}\Pi_{j_0k_0}\times \\
&\times\begin{Bmatrix} j_0 & j_1 & 1 \\ 1 & k_0 & l_1 \end{Bmatrix}\Bigg[C^{j_1,m_1}_{j_0,m_0,1,0}T^{l_1k_0}_{j_0m_0}+ \\
&+(\delta_{m_1,0}-1)^{j_1+m_1+l_1+1}C^{j_1,-m_1}_{j_0,m_0,1,0}\left(T^{l_1k_0}_{j_0m_0}\right)^*\Bigg]\boldsymbol{Y}^{l_1}_{j_1m_1}, \qquad \text{(A.47)}
\end{aligned}$$

and subsequently, for any $b = x, y, z$:

$$\begin{aligned}
T_{xb} =& \sum_{j=0}^{\infty}\sum_{m=0}^{j}(T_{xb})_{jm}Y_{jm} \\
=& \sum_{j=0}^{\infty}\sum_{m=0}^{j}\sum_{j_1=|j-1|}^{j+1}\sum_{m_1=0}^{j_1}\frac{(-1)^{j+j_1}}{\sqrt{2}}\frac{\Pi_{j_1}}{\Pi_j}\times
\end{aligned}$$

$$\times \Bigg[\left(C^{j,m}_{j_1,m_1,1,-1} - C^{j,m}_{j_1,m_1,1,1}\right) (T_b)^j_{j_1 m_1} + $$

$$+ (\delta_{m,0} - 1)^m \left(C^{j,-m}_{j_1,m_1,1,-1} - C^{j,-m}_{j_1,m_1,1,1}\right) \left((T_b)^j_{j_1 m_1}\right)^* \Bigg] Y_{jm}, \tag{A.48}$$

$$\begin{aligned} T_{yb} =& \sum_{j=0}^{\infty} \sum_{m=0}^{j} (T_{yb})_{jm} Y_{jm} \\ =& \sum_{j=0}^{\infty} \sum_{m=0}^{j} \sum_{j_1=|j-1|}^{j+1} \sum_{m_1=0}^{j_1} \frac{(-1)^{j+j_1}}{\sqrt{2}} \frac{\Pi_{j_1}}{\Pi_j} \times \\ & \times i \Bigg[\left(C^{j,m}_{j_1,m_1,1,-1} + C^{j,m}_{j_1,m_1,1,1}\right) (T_b)^j_{j_1 m_1} - \\ & - (\delta_{m,0} - 1)^m \left(C^{j,-m}_{j_1,m_1,1,-1} + C^{j,-m}_{j_1,m_1,1,1}\right) \left((T_b)^j_{j_1 m_1}\right)^* \Bigg] Y_{jm}, \end{aligned} \tag{A.49}$$

$$\begin{aligned} T_{zb} =& \sum_{j=0}^{\infty} \sum_{m=0}^{j} (T_{zb})_{jm} Y_{jm} \\ =& \sum_{j=0}^{\infty} \sum_{m=0}^{j} \sum_{j_1=|j-1|}^{j+1} \sum_{m_1=0}^{j_1} (-1)^{j+j_1} \frac{\Pi_{j_1}}{\Pi_j} \times \\ & \times \left[C^{j,m}_{j_1,m_1,1,0} (T_b)^j_{j_1 m_1} + (\delta_{m,0} - 1)^m C^{j,-m}_{j_1,m_1,1,0} \left((T_b)^j_{j_1 m_1}\right)^* \right] Y_{jm}, \end{aligned} \tag{A.50}$$

which are the desired Cartesian components of $\boldsymbol{T}$.

Bibliography

[1] Spencer, J.R. and Nimmo, F., 2013, Enceladus: An Active Ice World in the Saturn System. *Annual Review of Earth and Planetary Sciences*. 2013. Vol. 41, no. 1, p. 693-717. DOI 10.1146/annurev-earth-050212-124025. Annual Reviews

[2] Malamud, U. and Prialnik, D., 2013, Modeling serpentinization: Applied to the early evolution of Enceladus and Mimas. *Icarus*. 2013. Vol. 225, no. 1, p. 763-774. DOI 10.1016/j.icarus.2013.04.024. Elsevier BV

[3] Planetarynames.wr.usgs.gov, 2015, Planetary Names: Planet and Satellite Names and Discoverers. [online]. 2015. [Accessed 26 April 2015]. Available from: http://planetarynames.wr.usgs.gov/Page/Planets

[4] Cassini Solstice Mission, 2015, Enceladus. [online]. 2015. [Accessed 26 April 2015]. Available from: http://saturn.jpl.nasa.gov/science/moons/enceladus/index.cfm?pageListID=2

[5] Photojournal.jpl.nasa.gov, 2015, Photojournal: NASA's Image Access Home Page. [online]. 2015. [Accessed 1 May 2015]. Available from: http://photojournal.jpl.nasa.gov

[6] Maierová, P., 2006, *Vliv slapového zahřívaní na děje v nitrech ledových měsíců*. Bachelor thesis. Charles University in Prague.

[7] Matas, J., 1995, *Mantle Viscosity and Density Structure*. Diploma thesis. Charles University in Prague.

[8] Běhounková, M., Tobie, G., Choblet, G. and Čadek, O., 2012, Tidally-induced melting events as the origin of south-pole activity on Enceladus. *Icarus*. 2012. Vol. 219, no. 2, p. 655-664. DOI 10.1016/j.icarus.2012.03.024. Elsevier BV

[9] Einšpigel, D., 2015, *Ledové měsíce velkých planet*. Bachelor thesis. Charles University in Prague.

[10] Castillo-Rogez, J.C., Matson, D.L., Sotin, C., Johnson, T.V., Lunine, J.I. and Thomas, P.C., 2007, Iapetus' geophysics: Rotation rate, shape, and equatorial ridge. *Icarus*. 2007. Vol. 190, no. 1, p. 179-202. DOI 10.1016/j.icarus.2007.02.018. Elsevier BV

[11] Dougherty, M., Esposito, L. and Krimigis, S.M., 2009, *Saturn from Cassini-Huygens*. Dordrecht : Springer.

[12] Meyer, J. and Wisdom, J., 2008, Episodic volcanism on Enceladus: Application of the Ojakangas–Stevenson model. *Icarus*. 2008. Vol. 198, no. 1, p. 178-180. DOI 10.1016/j.icarus.2008.06.012. Elsevier BV

[13] Varshalovich, D.A., Moskalev, A.N. and Khersonskii, V.K., 1988, *Quantum theory of angular momentum*. Singapore : World Scientific Pub.

[14] Golle, O., Dumoulin, C., Choblet, G. and Čadek, O., 2012, Topography and geoid induced by a convecting mantle beneath an elastic lithosphere. *Geophysical Journal International*. 2012. Vol. 189, no. 1, p. 55-72. DOI 10.1111/j.1365-246x.2012.05364.x. Oxford University Press (OUP)

List of Tables

List of Abbreviations

CMB core-mantle boundary
LLRI long-lived radioactive isotopes

Attachments

Attachment 1: CD with the developed program and its necessary supplements.